INSTITUTE OF NATURAL AND APPLIED SCIENCE
UNIVERSITY OF ÇUKUROVA

MASTER THESIS

Tuğba KARAMAN

CALCULATION OF THE INTERCALIBRATION CONSTANTS FOR THE PROTOTYPE IV OF CASTOR DETECTOR

DEPARTMENT OF PHYSICS

ADANA, 2010

INSTUTUTE OF NATURAL AND APPLIED SCIENCE

ÇUKUROVA UNIVERSITY

CALCULATION OF THE INTERCALIBRATION CONSTANTS FOR THE PROTOTYPE IV OF CASTOR DETECTOR

Tuğba KARAMAN

A THESIS OF MASTER OF SCIENCE DEPARTMENT OF PHYSICS

We certify that the thesis titled above was reviewed and approved for the award of degree of Master of Science by board of jury on …./…./ 2010**.**

Signature	Signature	Signature
Prof. Dr. Ayşe POLATÖZ	Prof. Dr. Gülsen ÖNENGÜT	Asst.Prof.Dr. Nuri EMRAHOĞLU
SUPERVISOR	MEMBER	MEMBER

This MSc Thesis is performed in the Physics Department of the Institute of Natural and Applied Science of Çukurova University**.**
Registration Number:

Prof. Dr. İlhami YEĞİNGİL
Director
The Institute of Natural and Applied Science

This study was supported by Çukurova University's Scientific Research Fund.
Project Number: FEF2009YL027

Note: The usage of the presented specific declarations, tables, figures and photographs either in thesis or in any other reference without citation is subjected to "The Law of Intellectual and Art Products" numbered 5846 of Turkish Republic.

ABSTRACT

MSc THESIS

CALCULATION OF THE INTERCALIBRATION CONSTANTS FOR THE PROTOTYPE IV OF CASTOR DETECTOR

Tuğba KARAMAN

DEPARTMENT OF PHYSICS
INSTITUTE OF NATURAL AND
APPLIED SCIENCES UNIVERSITY OF ÇUKUROVA

Supervisor: Prof. Dr. Ayşe POLATÖZ
Year : 2010 Pages: 59
Jury : Prof. Dr. Ayşe POLATÖZ
Prof. Dr. Gülsen ÖNENGÜT
Asst. Prof. Dr. Nuri EMRAHOĞLU

CASTOR (Centauro and Strange Object Research) is a tungsten/quartz Cherenkov sampling calorimeter installed at the very forward region of the Compact Muon Solenoid (CMS) experiment at the Large Hadron Collider (LHC) at CERN. It covers the pseudo-rapidity range $5.1 < |\eta| < 6.6$ and is placed 14.38 m away from the interaction point. In order to test the performance of the CASTOR calorimeter, CASTOR Prototype IV was tested in the H2 beam line at CERN/SPS in 2008. Channel intercalibration was studied with E=50-300 GeV muons. In this thesis, inter-calibration constants were determined for the different channels using muons with E=300 GeV.

Key Words: LHC, CMS, HCAL, CASTOR.

ÖZ

YÜKSEK LİSANS

CASTOR KALORİMETRESİNİN IV. PROTOTİPİNİN KALİBRASYON SABİTLERİNİN HESAPLANMASI

Tuğba KARAMAN

ÇUKUROVA ÜNİVERSİTESİ
FEN BİLİMLERİ ENSTİTÜSÜ
FİZİK ANABİLİM DALI

Danışman : Prof. Dr. Ayşe POLATÖZ
Yıl : 2010 Sayfa:59
Jüri : Prof. Dr. Ayşe POLATÖZ
Prof. Dr. Gülsen ÖNENGÜT
Yrd. Doç. Dr. Nuri EMRAHOĞLU

CASTOR (Centauro and Strange Object Research), Büyük Hadron Çarpıştırıcısı'ndaki (BHÇ) Compact Muon Solenoid (CMS) deneyinin ileri bölgesine yerleştirilen ve Çerenkov ışıması ilkesine dayanan bir tungsten-kuartz örnekleme kalorimetresidir. Etkileşme noktasından 14.38 m uzaklığa konulmuştur ve $5.1<|\eta|<6.6$ pseudo-rapidite aralığını kaplamaktadır. CASTOR kalorimetresinin performansını test etmek amacıyla 2008 yılında CASTOR'un IV. prototipinin CERN/SPS H2 deney alanında hüzme testi yapılmıştır. Kanalların kalibrasyonu E=50-300 GeV'lik müonlarla çalışılmıştır. Bu tezde, hüzme testinde 300 GeV'lik muonlarla prototipin farklı kanallarının kalibrasyon sabitleri belirlenmiştir.

Anahtar Kelimeler: BHÇ, CMS, CASTOR.

ACKNOWLEDGEMENTS

I would like to thank my dear supervisor Prof. Dr. Ayşe Polatöz for her precious guidance and support during this study. It was pleasure for me to be her student and to work with her.

I also would like to thank Prof. Dr. Gülsen Önengüt, Prof. Dr. Eda Eşkut, Numan Bakırcı and Hüseyin Topaklı for their encouragement and guidance throughout my education.

I wish to thank all members of the CASTOR collaboration in particular, Igor Katkov for their valuable discussions and help.

I also wish to thank Mithat Kaya, Samim Erhan and Pawel de Barbaro for their valuable advice and suggestions, I am very pleased to have met them.

My deepest gratitude is to my dear mother Reşadiye Karaman, my brother Türker Karaman, my aunt Ümmü Görkem and her husband Prof. Dr İsmail Görkem for their unconditional love and encouragement throughout my life.

Thanks to my friends: Havva Yanış, Ayşe Şimşek, and Nilay Kantarcı for helping me during the my thesis.

I also would like to thank TAEK (Turkish Atomic Energy Authority) for their support during the time I have spent at CERN.

CONTENTS **PAGE**

ABSTRACT I
ÖZ II
ACKNOWLEDGEMENTS III
CONTENTS IV
LIST OF TABLES VI
LIST OF FIGURES VII
LIST OF SYMBOLS AND ABBREVATIONS XII
1. INTRODUCTION 1
2. LHC-CMS EXPERIMENT-CASTOR CALORIMETER 5
2.1. Large Hadron Collider (LHC) 5
2.2. Compact Muon Solenoid (CMS) 8
2.2.1. The Tracker 9
2.2.2. The Electromagnetic Calorimeter (ECAL) 10
2.2.3. The Hadronic Calorimeter (HCAL) 10
2.2.4. The Magnet 11
2.2.5. The Muon System 11
2.3. Forward Dedector of CMS Experiment: CASTOR 12
2.3.1. Introduction 12
2.3.2. CASTOR Components 16
2.3.2.1. Tungsten Plates 16
2.3.2.2. Quartz Plates 18
2.3.2.3. Air-Core The Lights Guides 19
3. CASTOR PROTOTYPES AND BEAM TESTS 21
3.1. Prototype I and Beam Test 2003 21
3.1.1. Absorber Tungsten and Sensitive Quartz Materials 22
3.1.2. Air-Core Light Guides 23
3.1.3. Photodetectors 23
3.1.4. Beam Test Results 24
3.1.4.(1). Energy Linearity and Resolution 24

3.2. Prototype II and Beam Test 2004 29
3.2.1. Beam Test Results 32
3.2.1.(1). Electron Beam 32
3.2.2.1.(1).a. Energy Response 32
3.2.1.(2). Muon Beam 35
3.3. Prototype III and Beam Test 2007 35
3.3.1. Muon Beam and Inter Calibrations of Channels 37
4. ANALYSIS AND RESULTS 40
4.1. Introduction 40
4.2. The H2 Beam Line 40
4.3. Beam Test 2008 of Prototype IV 43
4.3.1. Muon Beam and Intercalibration 43
5. CONCLUSION 56
REFERENCES 57
CURRICULUM VITAE 59

LIST OF TABLES **PAGE**

Table 3.1. Fit parameters obtained for the electromagnetic calorimeter prototype I (Aslanoglou et al., 2006) 27
Table 3.2. Inter-calibration constants for each channel, calculated using a run with a muon beam of 150 GeV (Aslanoglou et al., 2008) 39
Table 4.1. Properties of muon runs 44
Table 4.2. Intercalibration constants for each channel, calculated using a .. run with a muon beam of 300 GeV and equation 4.1 F_i corresponds to a Gaussian+Landau fit of the spectra for Saleve side 54
Table 4.3. Intercalibration constants for each channel, calculated using a .. run with a muon beam of 300 GeV and equation 4.1 F_i corresponds to a Gaussian+Landau fit of the spectra for Jura side 55

LIST OF FIGURES **PAGE**

Figure 1.1. Three generations of quarks, leptons and gauge bosons 2
Figure 2.1. The LHC layout 6
Figure 2.2. The fault of electrical connection between two magnets (shown in red) 7
Figure 2.3. The CMS detector 8
Figure 2.4. Event display at CMS Experiment 8
Figure 2.5. The CMS tracker 9
Figure 2.6. Muon system of CMS 12
Figure 2.7. Position of CASTOR Calorimeter in CMS (Panagiotou, 2007) 14
Figure 2.8. The photograph of the position of CASTOR Calorimeter in CMS (Panagiotou, 2008) 14
Figure 2.9. Longitudinal cross-sectional of 1/2 of CASTOR (EDR, 2007) 15
Figure 2.10. Front view of ½ of the CASTOR calorimeter design (EDR, 2007) 15
Figure 2.11. Construction drawing of the EM tungsten plates (CASTOR EDR, 2007)……..……16
Figure 2.12. Construction drawing of the HAD tungsten plates (CASTOR EDR, 2007)..... 17
Figure 2.13. Example of a tungsten plate 17
Figure 2.14. Construction drawings of the semi-octant quartz plate for the EM (CASTOR EDR, 2007)..... 18
Figure 2.15. Construction drawings of the semi-octant quartz plate for the HAD section (CASTOR EDR, 2007)..... 18
Figure 2.16. Example of a quartz plate 19
Figure 2.17. (a) and (b) Cross-section of the respectively EM and HAD light-guide with the PMT and base housing (CASTOR EDR, 2007)..... 19
Figure 2.18. Assembly of light guides onto W/Q sampling units..... 20
Figure 3.1. Left one: frontal view of prototype I. Right one: Lateral view of prototype I with one of the light guides (Aslanoglou et al.,2006) 21

Figure 3.2. Different Configuration options investigated in the 2003 beam test. The points A-O and 4-8 are scan locations used in calorimeter response uniformity studies (Aslanoglou et al., 2006) 22
Figure 3.3. The light guide for Prototype I, (Aslanoglou et al., 2006) 23
Figure 3.4. The two types of APDs used. Hamamatsu S8148, Advanced Photonix DUV (Aslanoglou et al., 2006) 24
Figure 3.5. Distributions of signal amplitudes in ADC channels for electron beam energies (20, 40, 80, 100, 150 and 200 GeV) impinging on the central point C of sector S1 (Quartz-Plate) using the Philips PMT (Aslanoglou et al., 2006) 25
Figure 3.6. Distributions of signal amplitudes in ADC channels for electron beam energies impinging on the central point C of sector S2 (Quartz-Fibre) using the Philips PMT (Aslanoglou et al., 2006) 25
Figure 3.7. Distributions of signal amplitudes in ADC channels for electron beam energies (20, 40, 80, 100, 150 and 200 GeV) impinging on .the central point C of sector J2 (Quartz-Fibre) using the Hamamatsu APD (Aslanoglou et al., 2006) 26
Figure 3.8. Distributions of signal amplitudes in ADC channels for electron beam energies(20, 40, 80, 100, and 150 GeV) impinging on the central point C of sector S1 (Quartz-Plate) using the Advanced Photonix APD (Aslanoglou et al., 2006) 26
Figure 3.9. Energy linearity in different sectors: (a) S1 (Philips PMT), (b) S2 (Philips PMT), (c) J2(APD1), (d) S1 (APD2) 28
Figure 3.10. Energy resolution in sectors: (a) S1 (Philips PMT), (b) S2 (Philips PMT), (c) J2 (APD1), (d) S1 (APD2). Two fits are shown: eq. (3.2) (solid); eq. (3.3) (dashed), with E given in GeV 29
Figure 3.11. The CASTOR prototype II. Before assembling the light-reading devices. The semi-octant geometry of the EM section and the octant geometry of the HAD section (Aslanoglou et al., 2007) 30

Figure 3.12. View of the W/Q-plates of the EM and HAD sections (bottom pictures) and of the light guides (upper picture) in the semi- octant (octant) geometry of the EM (HAD) sections respectively .of the CASTOR prototype-II (Aslanoglou et al., 2007) 31
Figure 3.13. Energy response of the EM calorimeter equipped with PMTs to 100 GeV electrons. The muons signal can also be seen (Aslanoglou et al., 2007)..... 33
Figure 3.14. Electromagnetic spectra for different beam energies (200 GeV and 20 GeV) for 4APD's and 6 APD's (Aslanoglou et al., 2007) 33
Figure 3.15. Energy response linearity (signal peak position versus beam energy) of the EM section, obtained with different light-reading devices: 4 APDs (left), 6 APDs (center), and PMTs (right) (Aslanoglou et al., 2007).... 34
Figure 3.16 Energy resolution of the EM section, obtained with the three readout configurations considered: 4 APDs (left), 6 APDs (center), and PMTs (right): 3-parameters fit Eq. (3.3) (top); 2-..parameters fit Eq. (3.2) (bottom) (Aslanoglou et al., 2007)..... 34
Figure 3.17. Energy spectra measured in the EM section of prototype II with a muon beam of 50 GeV energy and using two different PMTs: (a) Hamamatsu R7899, (b) RIE FEU187, and last one the sum of both (Aslanoglou et al., 2007) 35
Figure 3.18. The fully instrumented CASTOR octant prototype III installed on top of the moving table at the CERN/SPS H2 line 36
Figure 3.19. Schematic drawing of the beam-tests-2007 CASTOR prototype with the 28 readout units (RUs) indicated. The beam comes from the left impinging on the EM sections (Aslanoglou et al., 2008) 37
Figure 3.20. Energy spectra, before (top) and after (bottom) pedestal subtraction, measured in the two EM and first HAD sections of .the prototype III with a muon beam of 150 GeV energy impinging on the Saleve semi-octant equipped with Hamamatsu PMTs (Aslanoglou et al., 2008)..... 38

Figure 3.21. Energy spectra, before (top) and after (bottom) pedestal subtraction, measured in the EM section of the prototype III with a muon beam of 150 GeV energy impinging on the Jura semi-octant equipped with RIE FEU187 PMTs (Aslanoglou et al., 2008)..... 38
Figure 3.22. Intercalibration constants (F_i) of different channels in the Saleve .side semi-octant, derived from the muon energy spectra (Aslanoglou et al., 2008)..... 39
Figure 4.1. Schematic figure of the H2 beam line of the SPS at CERN (Aslanoglou et al., 2008) 40
Figure 4.2. WC-C and WC-D (Tali, 2009) 41
Figure 4.3. A view of MVB (Tali, 2009) 42
Figure 4.4. A view of sicintilation counters S1, S2 and S4 (Tali,2009) 42
Figure 4.5. ADC distribution of scintilation counters S1 & S2 & S4, first peak was fitted by a Gaussian for #48849 45
Figure 4.6. ADC distribution of scintilation counters S1 & S2 & S4, first peak was fitted by a Gaussian to select single hit for #48835 45
Figure 4.7. WC information for run # 48849 (Saleve sector) 46
Figure 4.8. WC information for run # 48835 (Jura sector) 46
Figure 4.9. ADC distribution of the MVB signals with pedestal trigger for run #48849)..... 47
Figure 4.10. ADC distribution of the MVB signals with pedestal trigger for run #48835)..... 47
Figure 4.11. For run #48849, beam profile onto the front face of the semi- octant calorimeter (Saleve sector) using the hits distribution from the WC-E, the left plot has not radius cut and the right one has 5 mm radius cut .. 48
Figure 4.12. For run #48835, beam profile onto the front face of the semi-octant calorimeter (Jura sector) using the hits distribution from the WC-E, the left plot has not radius cut and the right one has 5mm radius cut..... 48
Figure 4.13. Energy distribution, before cuts (a, b) and after cuts (c, d), measured in the two EM channels of prototype IV with a muon beam hitting on the Saleve side semi-octant for run #48849 49

Figure 4.14. Energy distribution, before cuts (a, b) and after cuts (c, d), measured in the first two HAD channels of prototype IV with a muon beam hitting on the Saleve side semi-octant for run #48849 50
Figure 4.15. Energy distribution, before cuts (a, b) and after cuts (c, d), . measured in the two EM channels of prototype IV with a muon beam hitting on the Jura side semi-octant for run #48835 51
Figure 4.16. Energy distribution, before cuts (a, b) and after cuts (c, d), measured in the first two HAD channels of prototype IV with a muon beam hitting on the Jura side semi-octant for run #48835 52
Figure 4.17. Intercalibration constants (*Fi*) of different channels in the Saleve side semi-octant, derived from the muon energy spectra 54
Figure 4.18. Intercalibration constants (*Fi*) of different channels in the Jura side semi-octant, derived from the muon energy spectra 55

LIST OF SYMBOL AND ABBREVATIONS

A : Nucleus
ADC : Analog to Digital Converter
ALICE : A Large Ion Collider Experiment
APD : Avalanche Photo Diode
ATLAS : A Toroidal LHC AparatuS
CASTOR : Centauro and STrange Object Research
CERN : European Nuclear Research Laboratory
CMS : Compact Muon Solenoid
ECAL : Electromagnetic Calorimeter
EM : Electromaagnetic
GeV : Giga Electron Volt
HAD : Hadronic
HB : Hadronic Barrel
HCAL : Hadronic Calorimeter
HE : Hadronic Encap
HERA : Hadron Electron Ring
HF : Hadronic Forward
HO : Hadron Outer
IP :Interaction Point
MeV : Million Electron Volt
LHC : Large Hadron Collider
LHCb : Large Hadron Collider Beauty Experiment
LINAC : Linear Accelerator
MVB : Muon Veto Back
p : proton
PS : Proton Synchrotron
Q : Quartz
QCD : Quantum Chroma Dynamics
PMT : Photo Multiplier Tube

P_T : Transverse momentum

RHIC : Relativistic Heavy Ion Collider

RU : Readout Unit

SM : Standard Model

SPS : Super Proton Sychrotron

SUSY : Supersymmetry

TeV : Billion Electron Volt

W : Tungsten

WC : Wire Chamber

X_0 : Radiation Length

λ_I : Interaction Length

η : pseudorapidity

1. INTRODUCTION

Everything in the universe is made of the same basic building block matter particles. Some particles were last seen only billionths of second after the Big Bang, however today; others form most of the matter around us. According to the particle physicists, matter is comprised twenty-four types of fundamental particle which are quarks and leptons with their anti-forms, in additional there are the gauge bosons which differ fundamentally from the quarks and leptons. Many fundamental particles do not exist under normal conditions in nature, but can be created and detected during energetic collisions of other particles, thus particle physics that analyze the elementary constituents of matter and radiation, and the interactions among them, is also called High Energy Physics.

The conditions just after the Big Bang were tried to recreate with powerful particle accelerators which speed up the particles almost to the velocity of light and collide them, so particle physicists can observe what happens in high energy collisions. The LHC (Large Hadron Collider) at CERN (European Organization for Nuclear Research Laboratory) is the largest accelerator in the world. LHC is constructed to have collisions at a center of mass energy of 14 TeV for proton-proton and 5.5 TeV for lead-lead collisions. Teams high energy particle physicist from around the world study the particles created in these collisions by using magnificent detectors at LHC. One of the detectors at LHC is CMS (Compact Muon Solenoid) which is designed to track or measure different type particles of coming from proton-proton and heavy ion collisions. The basic goals of the CMS experiment are finding Higgs boson, super symmetric particles beyond the Standard Model (SM), gravitons, and new phenomena like micro black holes

A quantum field theory called Standard Model has been developed to describe not only quarks and leptons but also their interactions. Sheldon Glashow discovered a way to combine the the electromagnetic and weak interactions as a first step towards Standard Model in 1963, the model was completed by Steven Weinberg and Abdus Salam in 1967. In this model Higgs mechanism gives rise to the masses of all the particles.

Although Standard Model (SM) describes the fundamental strong, weak, and electromagnetic interactions using gluons, W^-, W^+ and the Z^0 bosons and the photons as the force carrying particles, it can not answer some important questions; such as gravitational interaction, dark matter, non-zero neutrino masses, hierarchy problems, and unification of gauge coupling (Moortgat, 2004). In this model there are 6 quarks, 6 anti quarks and 6 leptons and 6 anti leptons as the building blocks of matter.

The quarks: up (u), down (d), charm (c), strange (s), top (t), bottom (b)

The leptons: electron (e), electron-neutrino (ν_e), muon (μ), muon-neutrino (ν_μ), tau (τ), tau-neutrino (ν_τ).

All of the fermions can be classified into 3 families and each family has 2 quarks and 2 leptons (Moortgat, 2004).

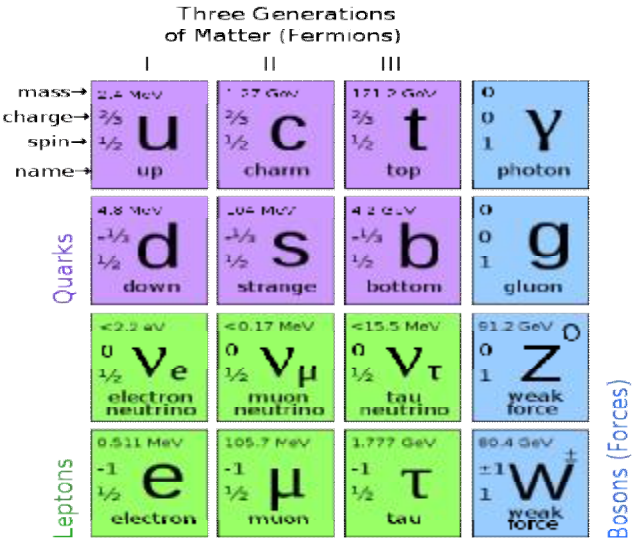


Figure 1.1. Three generations of quarks, leptons and gauge bosons

The two components of each family differ in one unit of electric charge: the quarks placed at the top row of the above figure 1.1 carry charge 2/3*e*, the other quarks placed at the bottom row have charge -1/3*e* where *e* is electric charge of an electron, and leptons have charges respectively 0 and -1*e* (Moortgat, 2004). The quarks also have a different sort of charge that is called color charge which comes in three varieties. These are: red, green, and blue. Moreover, anti-quarks have anti-

colors: anti-red, anti-green and anti-blue. That colour charge is relevant for their strong interactions, combining them inside hadrons. Hadrons are classified into 2 groups; baryons and mesons. 3 quarks make up baryons which are fermions, and a quark-anti quark pair makes up mesons which are bosons. Both baryons and mesons are called hadrons. The most well known baryons are proton and neutron that comprise most of the mass of the visible matter in the universe. Also each of the baryons has a corresponding antiparticle in which quarks are replaced by their corresponding anti-quarks. Mesons contribute both to the weak and strong interactions, those of them which are comprised of quarks with net electric charge also participate in the electromagnetic interaction.

Electromagnetic interactions take place between electrically charged particles. Electromagnetic forces involve exchange or production of photons (γ). Therefore, photons (γ) are carrier particles of these forces. Because photons are massless, the electromagnetic interactions have infinite range.

Weak interactions are responsible for the decay of massive quarks and leptons into lighter quarks and leptons. The carrier particles are the charged W^+ and W^- bosons and the neutral Z boson. They are massive (~ 100 GeV) and therefore the weak interaction is short ranged ($R \sim 10^{-17}$ cm) (Moortgat, 2004).

Strong interaction is seen between colour-charged quarks. Its carrier particles are called gluons (g). They have zero mass. So, like photon, they might be expected to have infinite range. However gluons, unlike photons, themselves carry a colour-charge and interact among each other (Moortgat, 2004) giving rise to a very short range.

Electroweak interaction; physicists educed that the weak and electromagnetic interactions have fundamentally equal strengths. This is due to the fact that strength of the interaction depends strongly on both the mass of force carrier particle and the distance of interaction. The difference between their observed strengths is because of huge difference in mass between the very massive W and Z particles and the massless photon. Although the Standard Model describes most of the phenomena in high energy physics, there are some phenomena which can not be explained by the Standard model.

The gravitational interaction is not defined in SM. A worse problem is that a unification of spin-1 gauge fields and spin-2 gravitation fields within a unique algebra has been proven to be not possible theoretically (Moortgat, 2004).

Many astrophysical observations point towards the existence of non-relativistic neutral, non-baryonic dark matter. A new candidate is needed for dark matter because neutrinos are not massive enough to explain the observations. (Moortgat, 2004).

Although the neutrinos are accepted as massless, recent experiments have showed that they have masses different from 0.

The hierarchy problem, is the large space between the energy scale at which the electroweak forces are unified and the energy scale (Planck scale) where quantum gravity becomes fundamental (Moortgat, 2004).

The unification of the gauge coupling strengths of the strong, weak and electromagnetic interactions should be possible at some energy scale if one thinks that three elementary interactions result from a local gauge theory with a higher fundamental symmetry (Moortgat, 2004).

Large Hadron Collider at CERN is built to observe Higgs boson and discover the physics beyond the SM. CMS is one of the two general purpose experiments on LHC and CASTOR is one of the subdetectors of CMS.

In this thesis, the general and technical features of CASTOR prototype IV are discussed and its calibration constants are calculated by using the data that were taken in the Beam Test 2008.

The second chapter gives information about LHC, CMS and CASTOR.

In the third chapter, the technical details, performance and general quality of CASTOR Prototypes (I, II and III) and data analysis of the previous beam tests are discussed.

In the fourth chapter, calibration constants were calculated with data that were taken in the Beam Test 2008

And finally in the last chapter, the analysis results are discussed.

2.1. LARGE HADRON COLLIDER (LHC)

CERN (European Organization for Nuclear Research) is the world's largest particles physics laboratory with several particle accelerators and other substructure. Many experiments have been conducted at CERN by international collaborations. Also, CERN is the birthplace of the World Wide Web (WWW). Most of the activities at CERN are currently directed towards building a new collider called the Large Hadron Collider (LHC) and the experiments for it. LHC is constructed in the 27 km circular LEP tunnel placed 100 m under the ground at the border of Switzerland and France. It is the highest energy particle accelerator used by physicists to analyse the fundamental building blocks of all matter. Inside the circular accelerator, two beams of hadrons, either protons or lead ions, will travel in opposite directions and will be accelerated. The LHC will be used to recreate the conditions just after the Big Bang, by colliding two beams head-on at a center of mass energy of 14 TeV. The particles created in the collisions will be detected using special detectors. LHC is expected to help physicists to answer the most significant questions of physics: What gives mass to particles? What is the nature of dark matter? How do we explain electroweak symmetry breaking?

In the LHC, there are four major experiments to answer these questions, ATLAS (A Large Torodial LHC Apparatus), CMS (Compact Muon Solenoid) , ALICE (A Large Ion Collider Experiment) and LHCb (Large Hadron Collider b-quark Experiment). CMS and ATLAS are general-purpose detectors to study multi particle collisions. Both detectors will search the extra dimensions, particle that could make up dark matter and Higgs boson, however their technical solution and designs of their detector magnet systems are different. At ALICE experiment, quark-gluon plasma will be studied with heavy ion (lead ions) collision. LHCb will determine the differences between matter and antimatter by studying B-mesons.

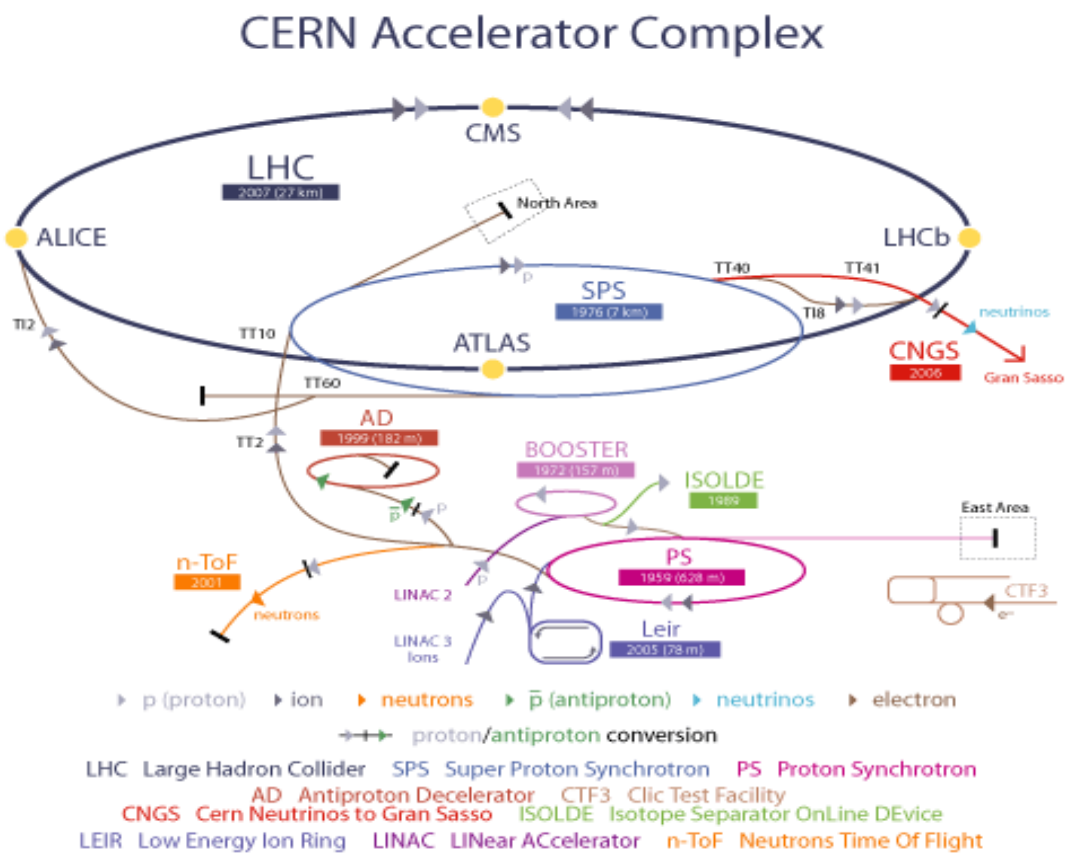


Figure 2.1. The LHC layout

The first beam (proton) in the Large Hadron Collider was successfully circulated around the 27 kilometers on 10 September 2008. Unfortunately, because of the fault of an electrical connection between magnets on 19 September 2008 (figure 2.2), it was not possible to have collisions. The LHC restarted at the end of the November 2009.

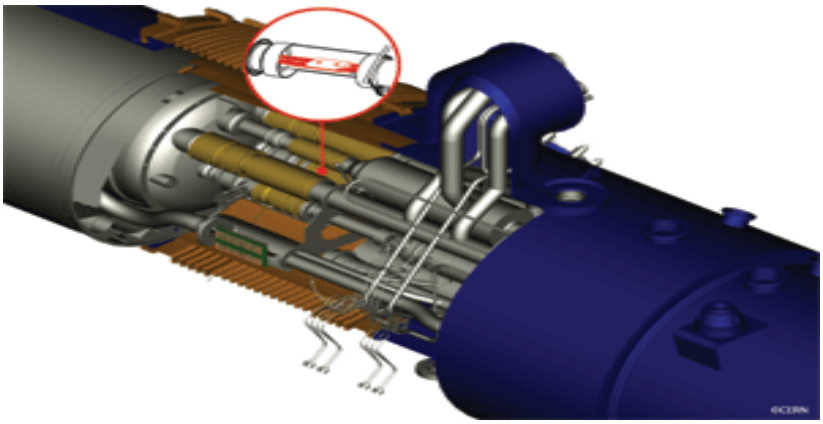


Figure 2.2. The fault of electrical connection between two magnets (shown in red)

Protons will start to accelerate with a Linear Accelerator (LINAC) which will raise their energy to 50 MeV, and then up to 1.4 GeV by a booster, and their energy will be increased to 25 GeV by the Proton Synchrotron (PS), and to 450 GeV by the Super Proton Synchrotron (SPS), and lastly protons will be injected into the LHC ring where protons will be accelerated up to 7 TeV. These accelerators are shown in Figure 2.1.

Proton bunches will collide every 25 ns or 40 million times per second. These bunches will have a transverse spread $\sigma_x = \sigma_y = 15$ μm and longitudinal spread 7.5 cm at the collision. The rate of a physics process can be calculated by

$$R = \sigma L \tag{2.1}$$

Where σ is the cross section, and L is Luminosity. The accelerator luminosity can be obtained by Equation (2.2). The maximum design luminosity of the LHC is 10^{34} cm^{-2} s^{-1}. (Gumus, 2008). L depends on the number of particles at each bunch (n_1 and n_2), f is circulation frequency, and inversely proportional to rms of beam radius σ_x and σ_y at the collision point:

$$L = \frac{f n_1 n_2}{4\pi\sigma_1\sigma_2} \tag{2.2}$$

2.2. COMPACT MUON SOLENOID (CMS)

The Compact Muon Solenoid (CMS) experiment will study a wide range of physics at terascale of energy, discover the Higgs boson if it exists, look for evidence of physics beyond the SM, SUSY or extra dimensions of space and understand how the universe came to be.

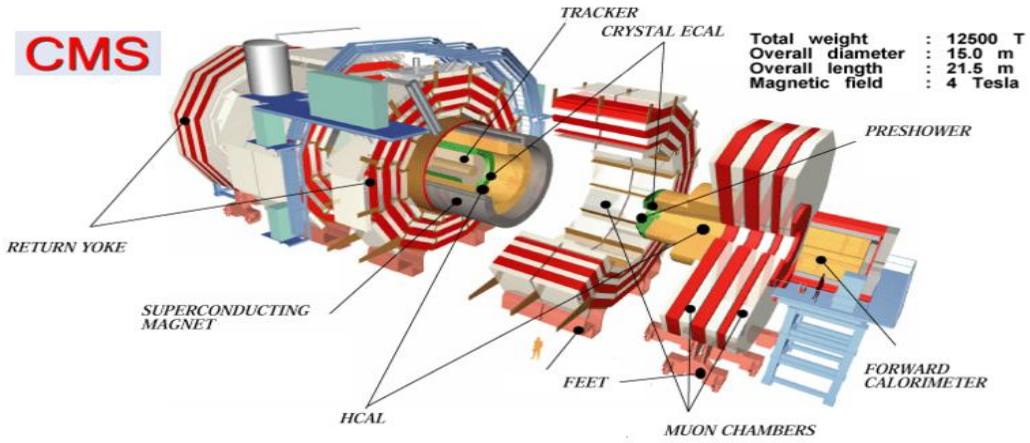


Figure 2.3. The CMS detector

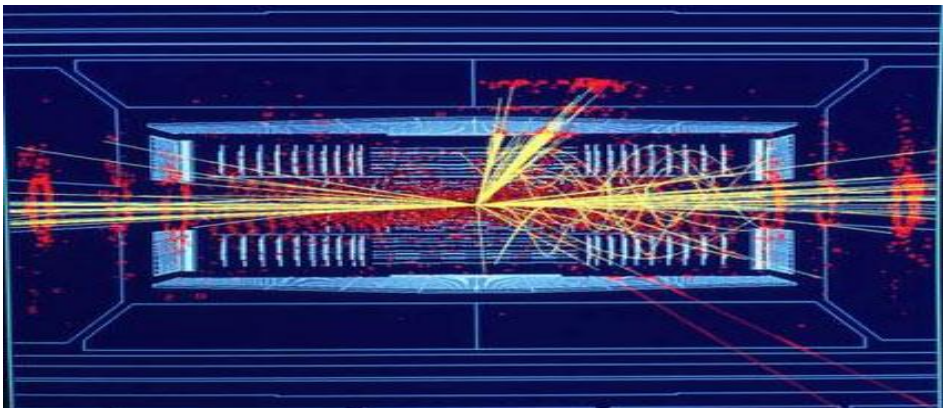


Figure 2.4. Event display at CMS Experiment

CMS detector was designed like a cylindrical onion with symmetry in the azimuthal angle and various layers were used in order to track and measure the energy and momentum. The layers of CMS from inside to outside: inner tracker, electromagnetic calorimeter (ECAL), hadronic calorimeter (HCAL), solenoid magnet, muon detector. There are forward detectors outside the magnet.

CMS detector has a length of 21.5 m (HF calorimeters excluded), overall diameter of 15 m and a total weight of 12500 tons. The detector has an almost 4π solid angle coverage and there are four main subdetectors which are the magnet, muon system tracking, electromagnetic and hadronic calorimeters. The central part of the detector is located in a 4 Tesla magnetic field which is parallel to the beam direction.

2.2.1. The Tracker

Tracker system is designed to reconstruct high P_T muons, electrons, and hadrons with high momentum resolution and efficiency and to measure the decay vertices of long-lived unstable particles. Segmented silicon sensors (pixels and strips) enable charged particles to be tracked and their momentum to be measured. Tracker covers the region $|\eta| < 2.5$. The tracking system is shown in Figure 2.5.

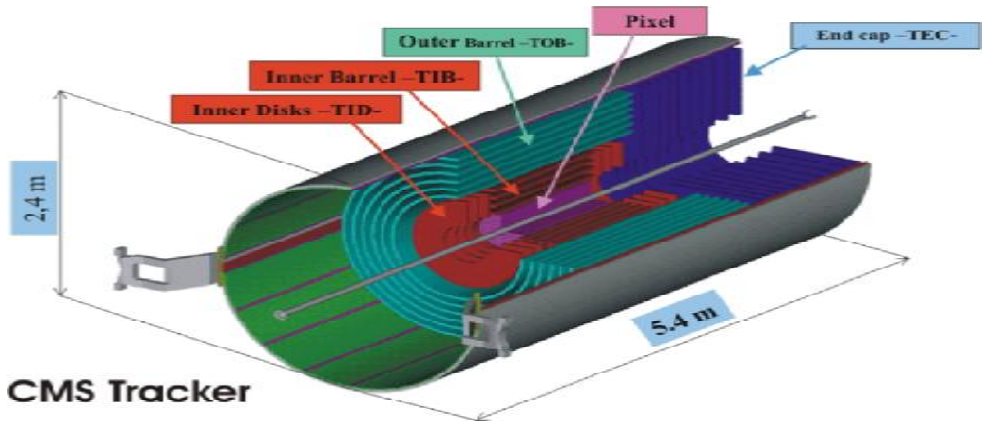


Figure 2.5. The CMS tracker

2.2.2. The Electromagnetic Calorimeter (ECAL)

The ECAL includes a barrel section and two endcaps. The cylindrical barrel consists of 61,000 crystals formed into 36 supermodules. Inner radius of the barrel section (EB) is 129 cm, covers the region $|\eta| < 1.48$. The EB has 36 supermodules and each supermodule contains four modules. Front face area of each lead tungstate crystal is 22×22 mm^2 and back face area is 26×26 mm^2. Its length is 230 mm (25.8 X_0). The endcaps (EE) are at a distance of 314 cm from the vertex, covering a pseudorapidity range of $1.5 < |\eta| < 3.0$. They have a front face cross section of 28.6×28.6 mm^2, a length of 220 mm, about 24.7 X_0.

The energies of photon and electrons is measured in ECAL which will play important role in the search for the Higgs, by measuring the photon decay mode, and by measuring electrons and positrons from the decay of W's and Z's coming from the H → ZZ^+ and H → WW decay chains.

2.2.3. The Hadronic Calorimeter (HCAL)

The Hadronic Calorimeter (HCAL) measures the energy of hadrons which are particles made of quarks and gluons such as protons, neutrons, and pions. Additionally it provides indirect measurement of the presence of non-interacting, uncharged particles such as neutrinos. Measuring these particles is important as they can tell us if new particles such as the Higgs boson or supersymmetric particles have been formed. The HCAL include four subdetectors which are Hadron barrel (HB), Hadron endcap (HE), Hadron outer (HO) and Hadron forward (HF). HB covers the η range $-1.4 < |\eta| < 1.4$ and the HCAL endcaps (HE) cover the pseudorapidity range $1.3 < |\eta| < 3.0$. They are the sampling calorimeters which consist of plastic scintillators as active material inserted between copper absorber plates, which are placed between the ECAL and the magnet. The HF calorimeters, the last subdetector of HCAL, are placed ~11 m away from the interaction point. The HF calorimeter improves the measurement of the missing transverse energy and allows very forward jets to be identified and reconstructed. The HF calorimeter is located at $3.0 < |\eta| < 5.0$. It uses

the quartz fibers as the active medium. There are two HFs at both sides of CMS. Each HF has an active radius of 1.4 m and consists of iron absorbers, fibers embedded into the absorbers, and phototubes. Fibers have two different lengths to differentiate between shower processes. Longer fibers will provide light from electromagnetic and hadronic showers in the absorber. Shorter fibers will only see the hadronic showers. The long and the short fibers are read out by separate PMTs.

2.2.4. The Magnet

The magnet is a long superconducting solenoid of length 13 m and inner diameter 5.9 m. It produces a magnetic field of 4 T. The magnetic flux is returned via a 1.8 m thick saturated iron yoke. The yoke consists two endcaps and five barrel rings. The aim of the magnet is to achieve reconstruction of 1 TeV muons with a 15% P_T (transverse momentum) resolution. The connection between P_T and the magnetic field is shown by

$$P_T = 0.3BR \tag{2.3}$$

where R is the radius of the curvature of the particle in m and B is the magnetic field in tesla (Gumus, 2008)

2.2.5. The Muon System

Muon system plays an important role in physics. One of the design aim of the CMS is identifying muons correctly and reconstructing their momentum precisely. The muon system was made of three detectors which are Drift Tubes (DT) in the barrel region, Cathode Strip Chambers (CSC) in the endcap region, and Resistive Plate Chambers (RPC) in both the barrel and endcap regions. Figure 3.6 shows the layout of the muon System. The DT and CSC will provide very accurate and precise position measurements while RPC provide precise time measurements (Gumus, 2008).

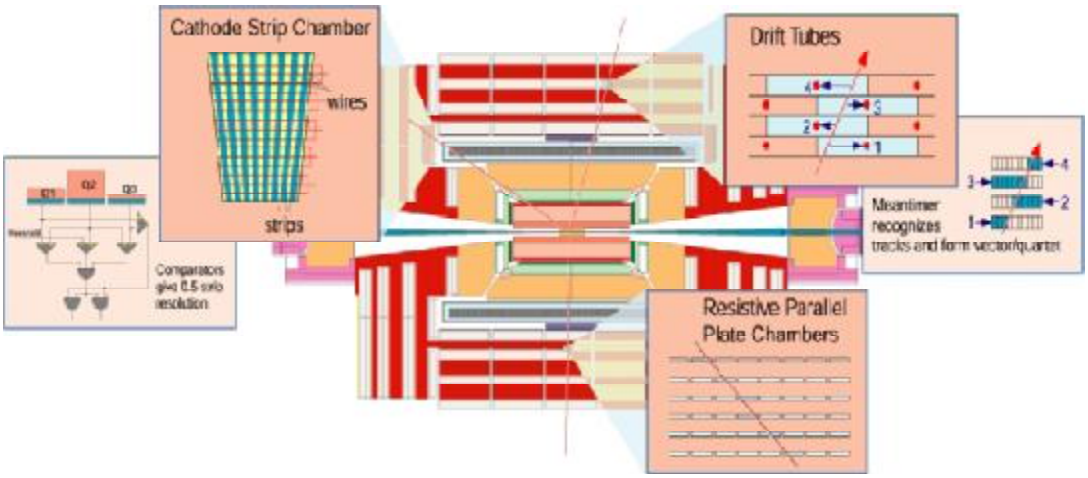


Figure 2.6. Muon system of CMS

2.3. FORWARD DETECTOR OF CMS EXPERIMENT: CASTOR

2.3.1. Introduction

Modern high energy heavy-ion experiments are focused principally on the study of the high temperature baryon-free mid-rapidity region. The potentially very rich field of novel phenomena is expected to be investigated at the forward phase space at the LHC. Also studying particle production at small angles is encouraged by some experimental results which derive from accelerator experiments and cosmic rays. The suggested new form of QCD matter named the Colour Glass Condensate (CGC), motivated by HERA (Hadron Electron Ring) and RHIC (Relativistic Heavy Ion Collider) data should be studied at the LHC.

The abnormal observations registered in cosmic ray experiments led to the CASTOR (Centauro And Strange Object Research) project. The physics program of this project has been recently enriched and CASTOR will contribute to heavy ion studies additionally to diffractive and low-x physics in proton-proton (pp) and proton-nucleus (pA) collisions. Thus, CASTOR will provide the opportunity to test a

nonperturbative region of QCD at Bjorken-*x* (which is a deep inelastic scattering variable and the value of the Bjorken-*x* gives us information about how much of the proton momentum is carried by the gluon or quark) as small as ~10^{-6} -10^{-7}.

Exotic phenomena discovered in cosmic ray experiments inspired the CASTOR project. In the detectors used in cosmic experiments, sandwiches of lead absorbers and sensitive layers make up the top and bottom chambers. While the bottom chamber principally detects the hadrons, the top chamber principally detects the electromagnetic component which occurs in the interaction of a cosmic ray particle with an air nucleus. In a "normal" event that is registered in such a device the hadronic component constitutes not more than 30 % of the total visible energy. Therefore, events with a different ratio were a big surprise. The confusing events, called Centauros were characterized by a strongly decreasing electromagnetic component and abnormal hadron excess and have been observed at energies above 10^{15} eV (Gladysz-Dziadus, 2006).

CASTOR, a Cherenkov-type calorimeter is constructed for the very forward region of CMS. CASTOR calorimeter has a shape of an octagonal cylinder in two halves, covers the pseudo rapidity range $5.2< |\eta| < 6.6$ is located at $-z = 14.47$ m from the interaction point (IP), just after the Hadronic Forward (HF) calorimeter and T2, a tracking station of TOTEM experiment. CASTOR calorimeter includes tungsten plates as absorber and fused silica quartz plates as active medium, both are placed at 45^{o} with respect to the beam axis.

The CASTOR calorimeter is an electromagnetic (EM) and hadronic (HAD) detector with 16 sectors azimuthally symmetrical around the beam pipe. It is also longitudinally segmented into 14 sections, EM section has 2 parts and HAD section has 12 parts. Total depth of the calorimeter is 10 interaction lengths, $\lambda_{I.}$ Depth of the EM sections is 2×10=20 radiation lengths, X_0 and EM section consists of 2×16 channels. Depth of HAD section is 12×0.77= 9.24 $\lambda_{I.}$ and HAD section consists of 12x16 channels. The signal is the Cherenkov light produced by the passage of the charged particles through the quartz medium. These W/Q-layers are inclined at 45^{o} from the beam direction, in order to maximize the Cherenkov light output. Figures 2.7 and 2.8 show the location of CASTOR in the CMS forward region.

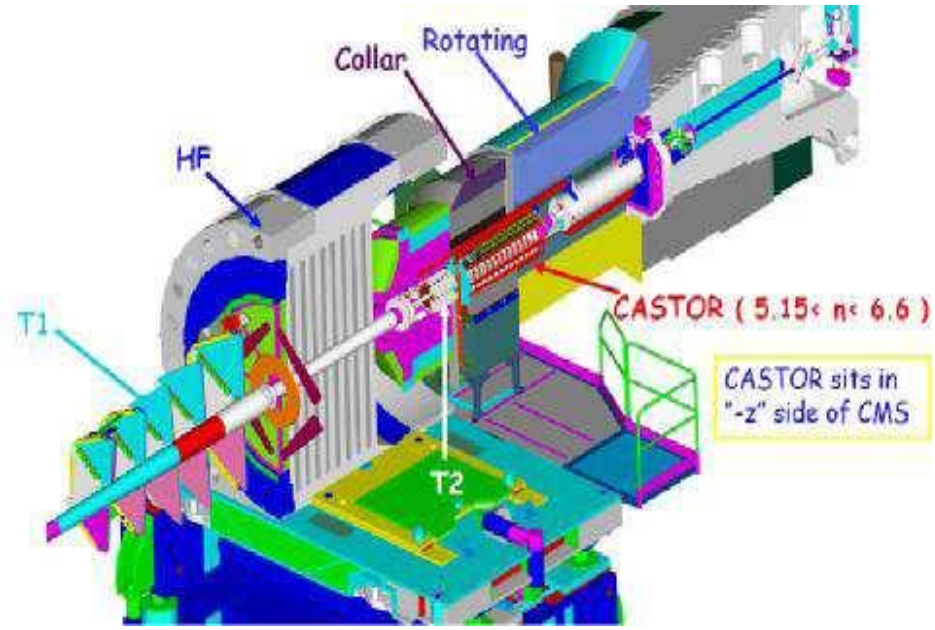


Figure 2.7. Position of CASTOR Calorimeter in CMS (Panagiotou, 2007)

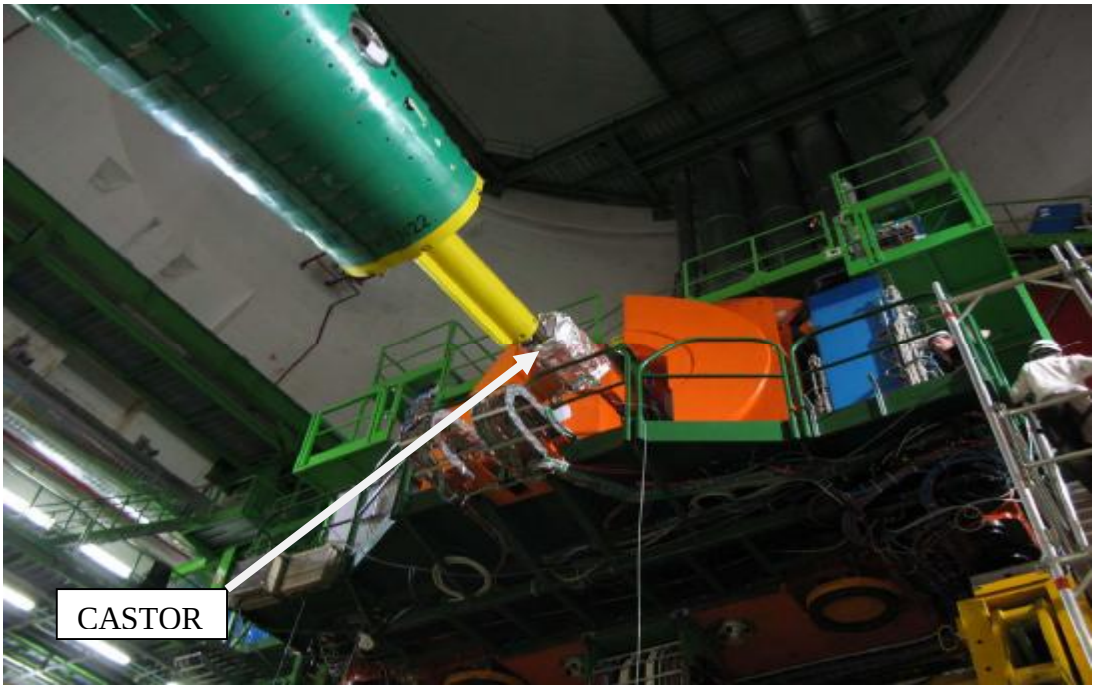


Figure 2.8. The photograph of the position of CASTOR Calorimeter in CMS (Panagiotou, 2008).

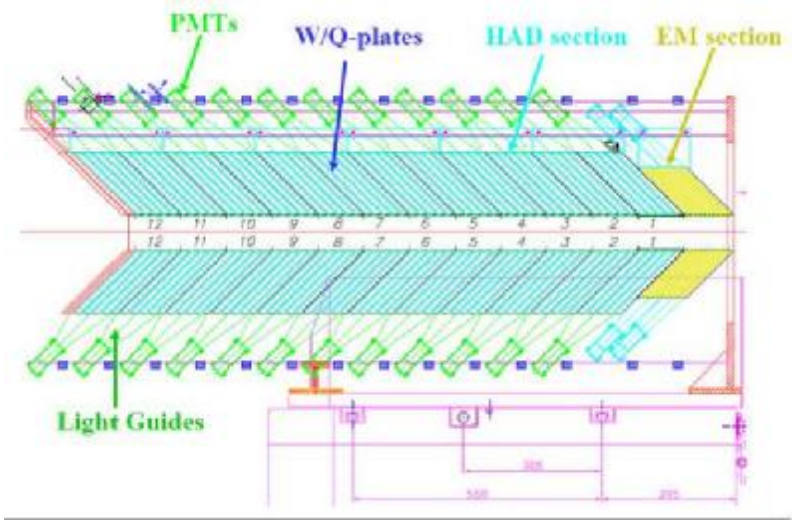


Figure 2.9. Longitudinal cross-sectional of 1/2 of CASTOR (EDR, 2007).

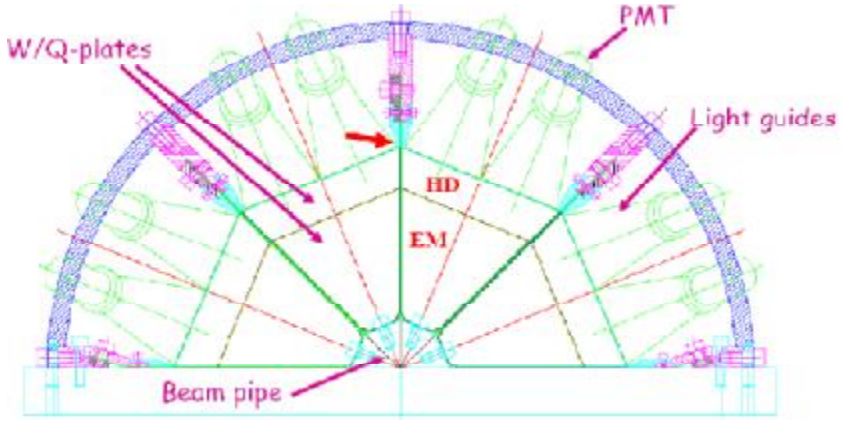


Figure 2.10. Front view of ½ of the CASTOR calorimeter design (EDR, 2007).

Figure 2.10 shows the front view of the calorimeter design. It has four octants forming half of the calorimeter that is constructed in two semi-circular sections of 4 octants, to be positioned around the fixed beam pipe. Also figure 2.9 shows longitudinal cross sectional of half calorimeter design.

2.3.2. CASTOR Compenents

2.3.2.1. Tungsten Plates

The density of the tungsten plates is 18.5±0.2 g/cm^3. So they contain 97% W, 1.3% Fe and 1.7% Ni. Thickness is 5 mm and 10 mm for EM and HAD sections respectively but the effective thickness increases to 7.07 mm for EM section, 14.14 mm for HAD section at 45^o inclination. Figure 2.11 and 2.12 shows the octant trapezoidal shape and dimensions of the tungsten plates. The CERN Metrology Section measured the geometry, dimensions, consistency and density of samples of the W-plates (CASTOR EDR, 2007). One of the tungsten plates is shown in Fugure 2.13.

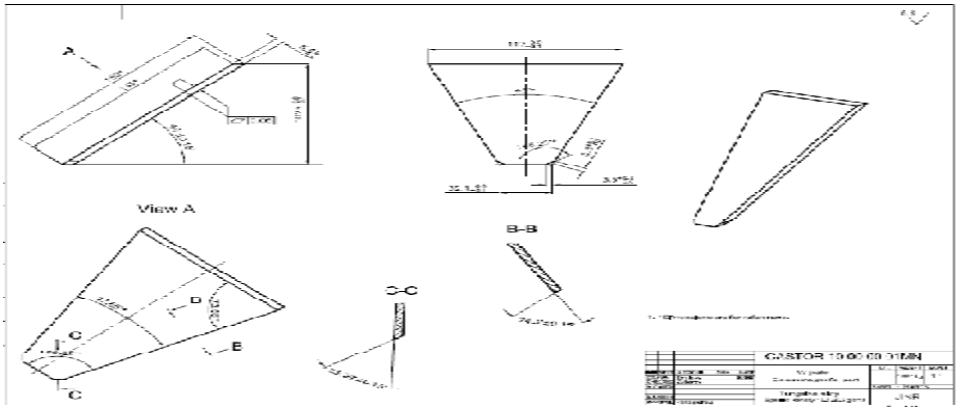


Figure 2.11. Construction drawing of the EM tungsten plates (CASTOR EDR, 2007)

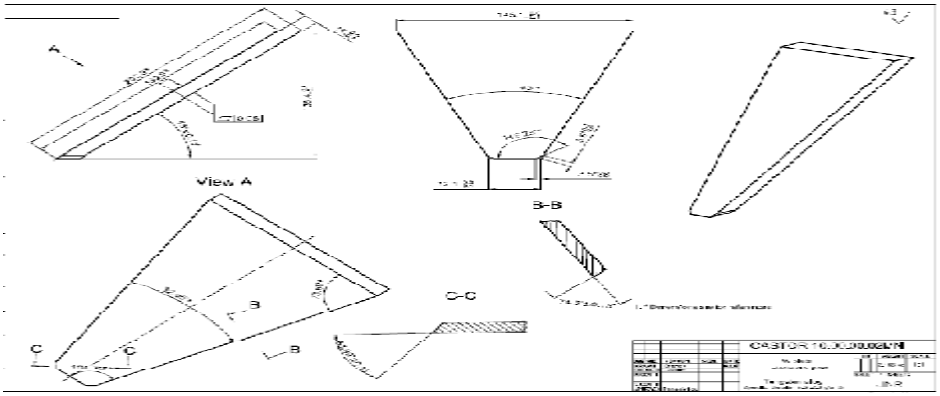


Figure 2.12. Construction drawing of the HAD tungsten plates (CASTOR EDR, 2007)



Figure 2.13. Example of a tungsten plate.

2.3.2.2. Quartz Plates

The quartz plates are designed in a semi-octant geometry and define the 16-fold azimuthal segmentation of the calorimeter. Figure 2.14 and 2.15 show the semi-octant construction designs of the EM and HAD Q-plates. Their thicknesses are 2 mm and 4 mm for the EM and HAD sections respectively. The two semi-octants Right, Left (R, L) are positioned side by side along their vertical side. They are optically separated by a thin Al foil. The light guides are placed on top of the 5 tungsten/quartz plates to form the RU in both the EM and HAD sections. Also, Tyvek paper is used as an emitter for small fraction of light that may escape through

the surfaces at incidences smaller than the total reflection angle. Moreover tyvek protects the polished quartz plate's interface with tungsten. Figure 2.16 shows one of the tungsten plates.

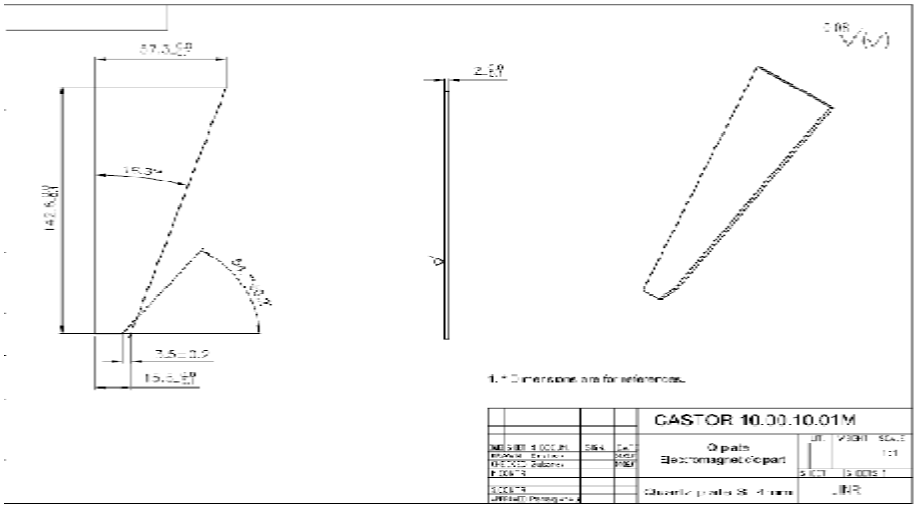


Figure 2.14. Construction drawings of the semi-octant quartz plate for the EM (CASTOR EDR, 2007) .

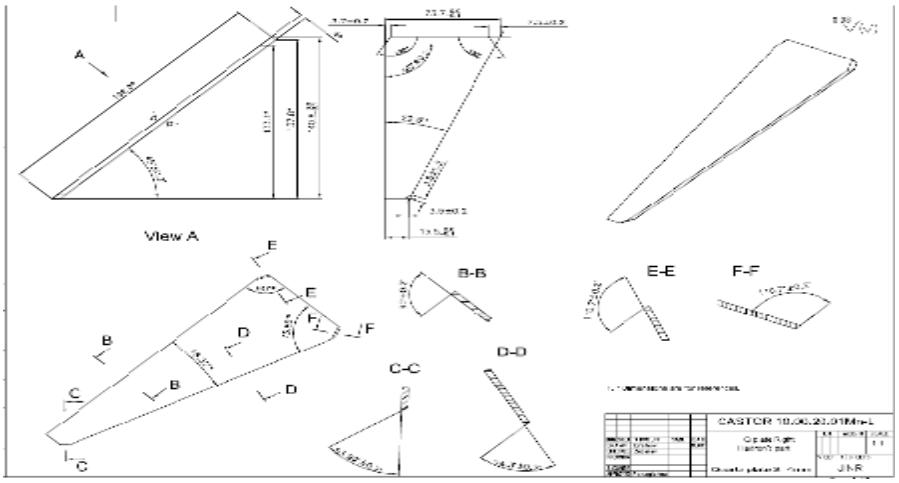


Figure 2.15. Construction drawings of the semi-octant quartz plate for the HAD section (CASTOR EDR, 2007).

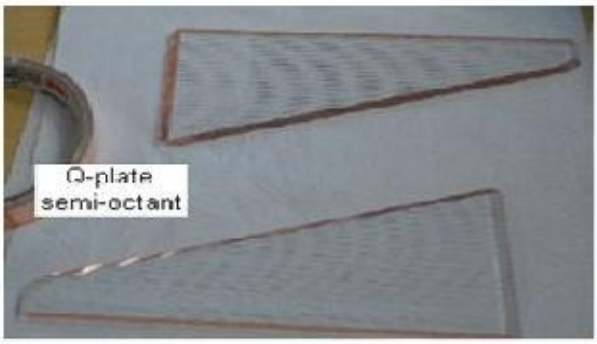
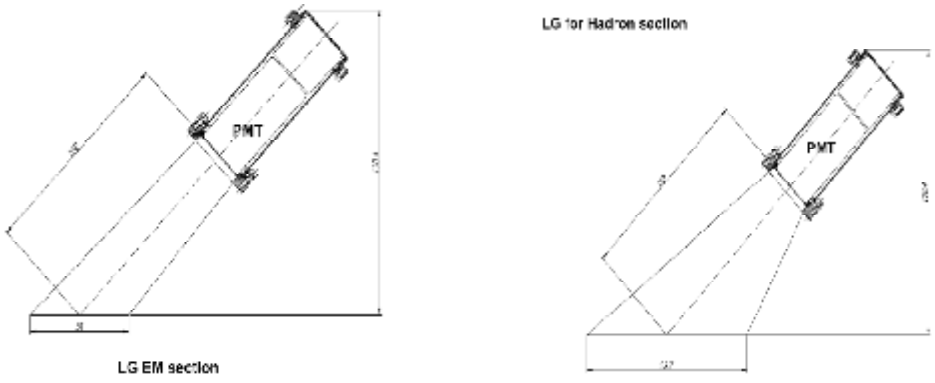


Figure 2.16. Example of a semi-octant quartz plate (Tali,2009)

2.3.2.3. Air-Core The Light Guides

The Cherenkov light is produced and collected and then transmitted to the PMTs by air-core light guides. The efficiency of light transmission and its dependence on the light-source position are crucial parameters, which characterize the light guide and significantly affect the performance of the calorimeter. The design and dimensions of the air-core light guides for the electromagnetic and hadronic sections are obtained from Monte Carlo simulations. Figure 2.17 shows the construction drawings of the EM and HAD light guides, respectively. For the transmission of the Cherenkov light, the inside walls of the light guides are covered with a reflecting foil.



(a) (b)

Figure 2.17. (a) and (b) Cross-section of the respectively EM and HAD light-guide with the PMT and base housing (CASTOR EDR, 2007).

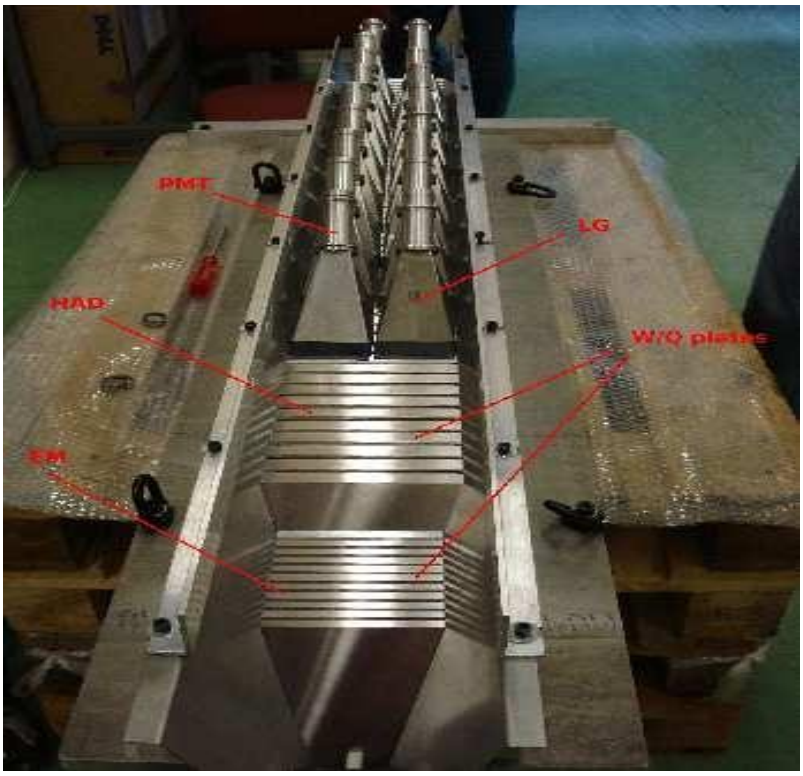


Figure 2.18. Assembly of light guides onto W/Q sampling units

Figure 2.18 shows assembly of light-guides and PMTs onto tungsten/quartz sampling units.

3. CASTOR PROTOTYPES AND BEAM TESTS

3.1. Prototype I and Beam Test 2003

The first successful performance study of the CASTOR calorimeter was conducted with Prototype-I that was constructed and tested with electron beams in the H4 line at CERN/SPS in the summer 2003. Figure 3.1 shows the general view of the prototype-I. The purpose of this beam test was to investigate and compare the performance of different combinations of structures for the active material of the calorimeter (quartz plates and fibres), different types of light-guide reflecting materials (glass and foil reflectors) and photodetector devices (photomultipliers, and avalanche photodiodes). Different sectors of the calorimeter were setup with various quartz active materials and with different photodetector devices (PMTs, APDs). Prototype I included only an Electromagnetic (EM) section seen in figure 3.1 (Aslanoglou et al., 2006; EDR, 2007). In order to maximize the Cherenkov light output, the tungsten (W) and quartz (Q) plates were inclined at 45° with respect to the beam axis. (Aslanoglou et al, 2006).

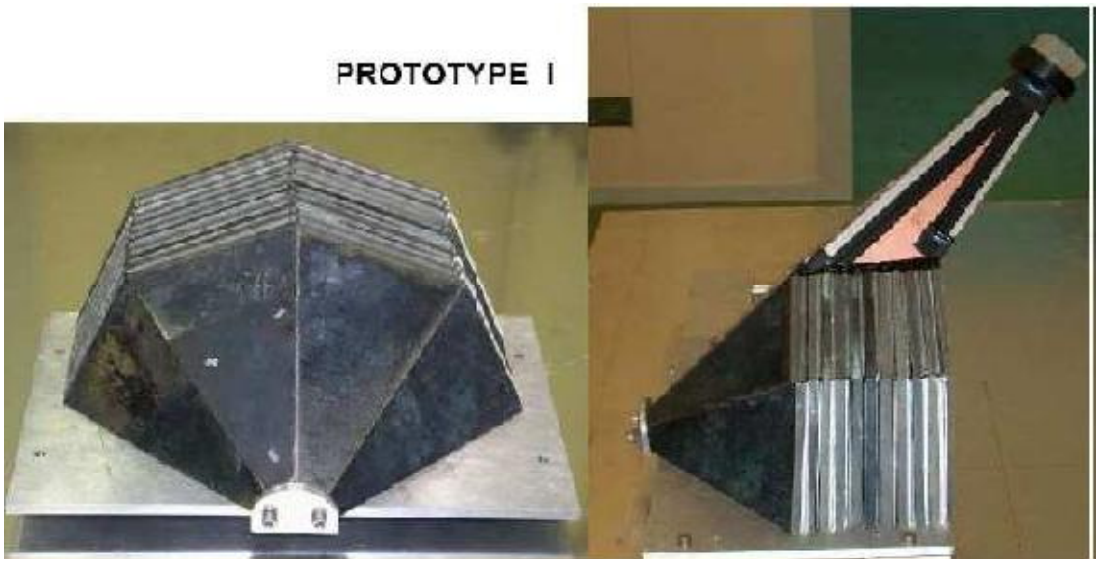


Figure 3.1. Left one: frontal view of prototype I. Right one: Lateral view of prototype I with one of the light guide (Aslanoglou et al., 2006).

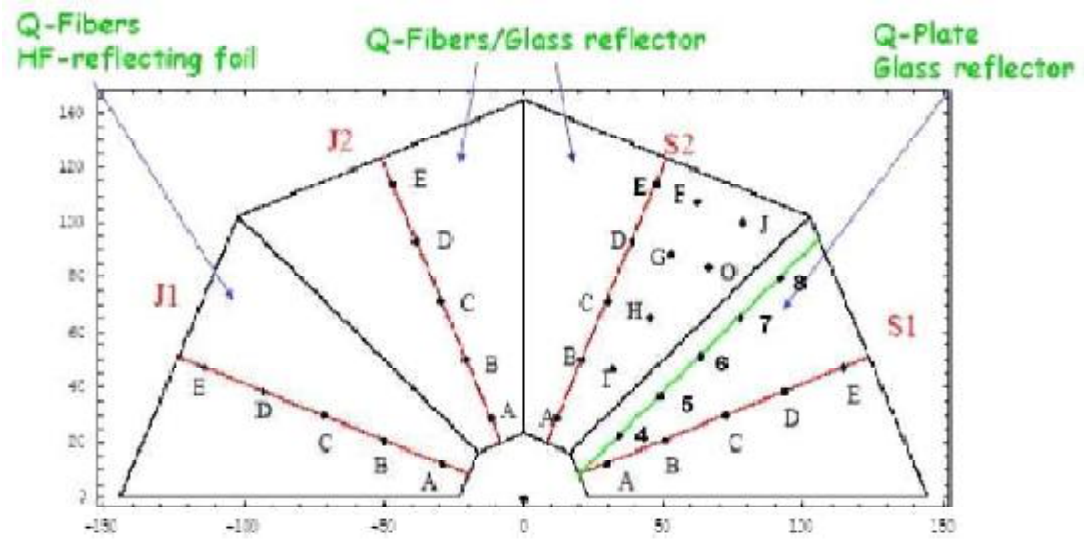


Figure 3.2. Different Configuration options investigated in the 2003 beam test. The points A-O and 4-8 are scan locations used in calorimeter response uniformity studies (Aslanoglou et al., 2006).

3.1.1. Absorber Tungsten and Sensitive Quartz Materials

The prototype-I is azimuthally divided into 4 octants and longitudinally segmented into 10 W/Q layers as shown in Fig. 3.1. The total length of each sector was 19.86 X_o and the effective length of each W-plate was 7.07 mm. Density of W-plates was ~19.0 g/cm^3 ignoring the contribution of the quartz material. The calorimeter response and relative energy resolution were studied for quartz fibres (Q-F) and quartz plates (Q). Four octant readout units of the calorimeter were tested, arranged side-by-side in four azimuthal sectors. Each readout unit consisted of 10 sampling units so each sampling unit for sectors J1, J2, S1and S2 that are shown in Fig. 3.2 was comprised of a 5 mm thick tungsten plate and three plates of 640 μm thick quartz fibres. The quartz fibres were produced by Ceram Optec and featured 600 μm pure fused silica core with a 40 μm polymer. For sector S1, the sampling unit consisted of a 5 mm thick tungsten plate and one 1.8 mm thick quartz plate. Both types of quartz active material, fiber or plate, had about the same effective thickness. The filling ratio was 30% and 37% for the quartz fibers and quartz plates, respectively (Aslanoglou et al., 2006).

3.1.2 Air-Core Light Guides

The air-core light-guide used for the CASTOR Prototype I which was made of Cu-plated 0.8 mm PVC is shown in Figure 3.3. Two types reflecting materials were used for the inner walls of the light guide for the light transmittance: float-glass with evaporations of AlO and MgFr with a thickness of 0.5 mm and a Dupont polyester film reflector coated with AlO and enhancing the dielectric layer stack SiO_2 +TiO_2 (HF reflecting foil).

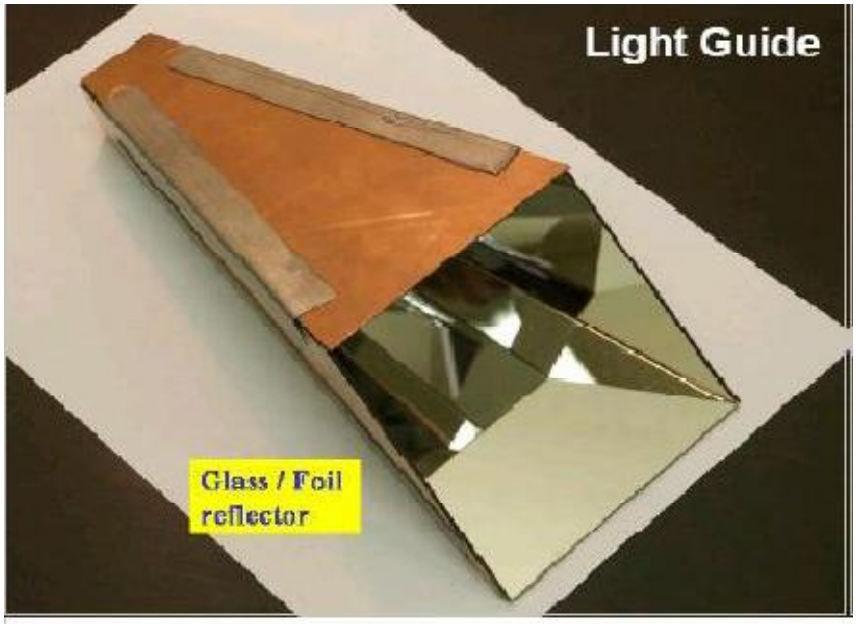


Figure 3.3. The light guide for Prototype I, (Aslanoglou et al., 2006)

3.1.3. Photodetectors

Prototype-I had two different types of light-sensing devices: Avalanche Photodiodes (APDs) and photomultipliers (PMTs).

Two different types of Avalanche Photodiodes (APDs): Hamamatsu S8148 (APD1) and Advanced Photonix Deep-UV (APD2) are shown in figure 3.4 as well as two different types of photomultipliers (PMTs): Hamamatsu R374 and Philips XP2978 were tested. Four Hamamatsu APDs, each 5×5 mm^2, were used, in a 2×2

mm^2 matrix with total area of 1 cm^2. The Advanced Photonix DUV APD had an active area of 2 cm^2. The Hamamatsu and Philips PMTs both have an active area of 3.1 cm^2.



Figure 3.4. The two types of APDs used. Hamamatsu S8148, Advanced Photonix DUV (Aslanoglou et al., 2006)

3.1.4. Beam Test Results

The Prototype-I was placed on a platform movable with respect to the electron beam in both horizontal and vertical directions. Two wire chambers, telescopes as well as two crossed finger scintillator counters were positioned in front of the calorimeter to determine the electron impact point.

3.1.4.(1). Energy Linearity and Resolution

The linearity and resolution of the prototype-I were analyzed as a function of energy, when the central point C (figure 3.2) in different azimuthal sectors have been exposed to electron beams of energy 20, 40, 80, 120,150, 200 GeV. After introducing the cuts accounting for the profile of the beam, the distributions of signal amplitudes are symmetrical and their Gaussian fits are shown in figures 3.5-3.8.

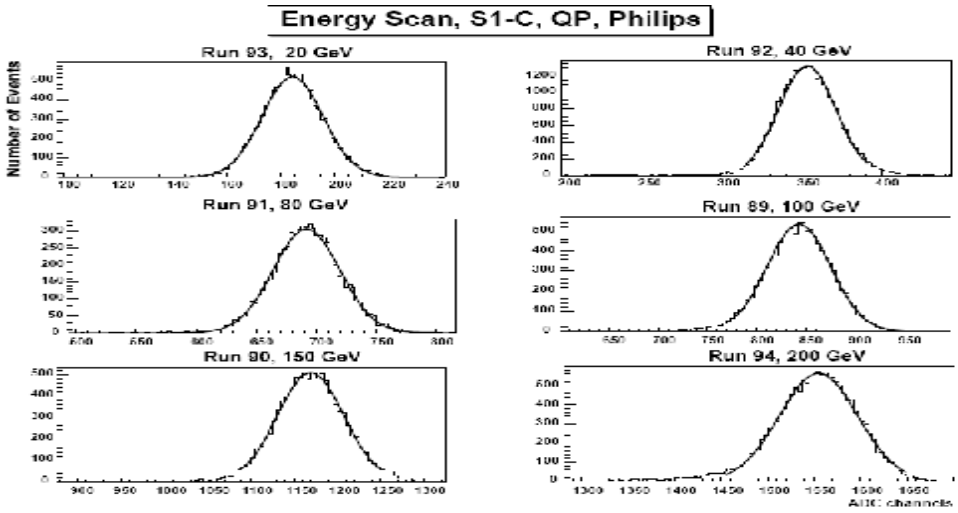


Figure 3.5. Distributions of signal amplitudes in ADC channels for electron beam energies (20, 40, 80, 100, 150 and 200 GeV) impinging on the central point C of sector S1 (Quartz-Plate) using Philips PMT (Aslanoglou et al., 2006).

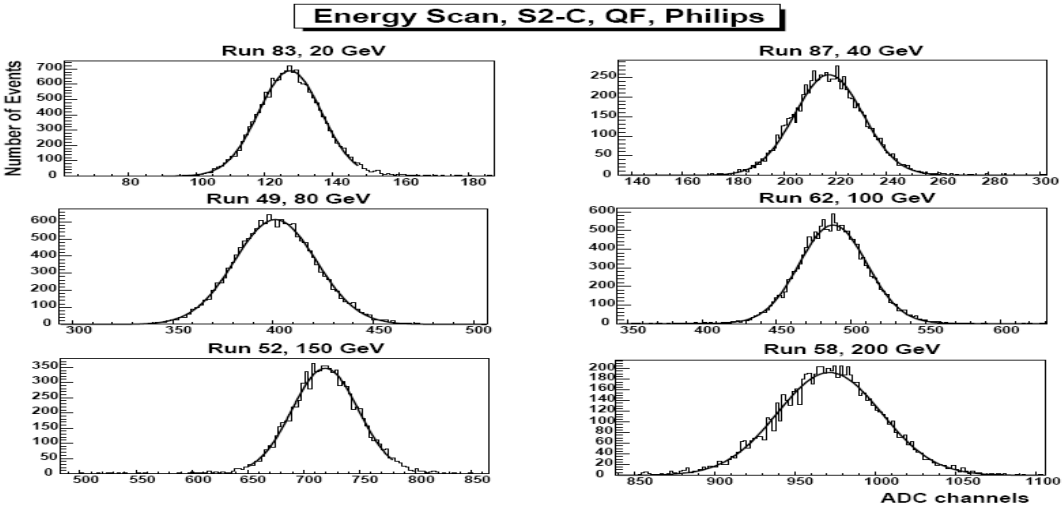


Figure 3.6. Distributions of signal amplitudes in ADC channels for electron beam energies impinging on the central point C of sector S2 (Quartz-Fibre) using Philips PMT (Aslanoglou et al., 2006).

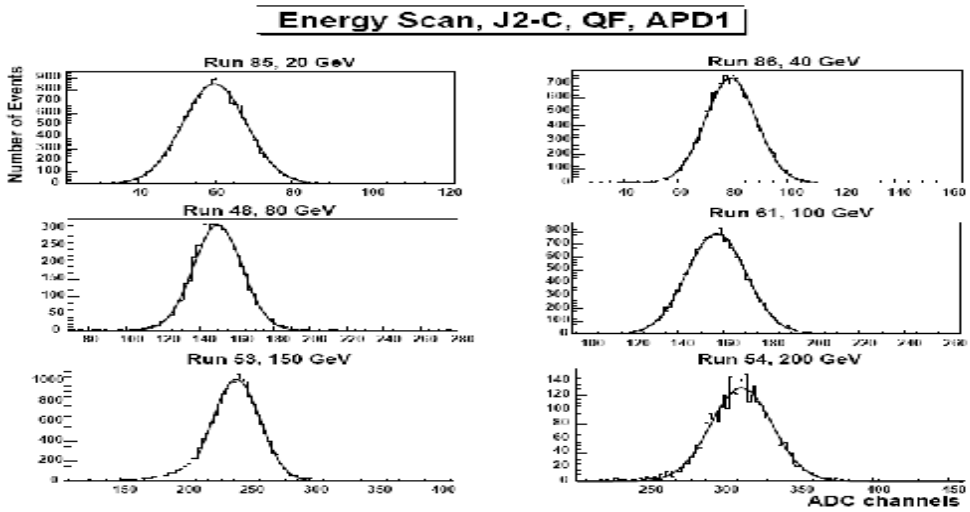


Figure 3.7. Distributions of signal amplitudes in ADC channels for electron beam energies (20, 40, 80, 100, 150 and 200 GeV) impinging on the central point C of sector J2 (Quartz-Fibre) using Hamamatsu APD (Aslanoglou et al., 2006).

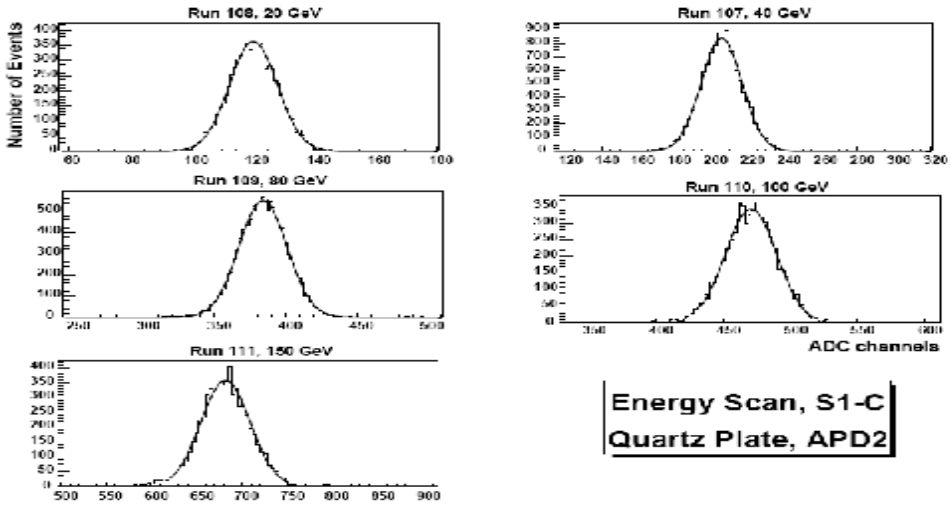


Figure 3.8. Distributions of signal amplitudes in ADC channels for electron beam energies(20, 40, 80, 100, and 150 GeV) impinging on the central point C of sector S1 (Quartz-Plate) using Advanced Photonix APD (Aslanoglou et al., 2006).

In Figure 3.9, mean response of different sectors of the calorimeter is shown as a function of energy. It seems linear in the range explored. The average signal

amplitude, expressed in units of ADC channels, can be satisfactorily fitted by the following formula:

$$ADC = a + b \times E \quad (3.1)$$

where the energy E is in GeV. The fitted values of the parameters for each configuration are shown in Fig. 3.9 and are tabulated in Table 3.1.The parameter a gives the pedestal value which is roughly the same for all analyzed configurations. The ADC pedestal values measured for the various configurations considered are shown in table 3.1.

Table 3.1. Fit parameters obtained for the electromagnetic calorimeter prototype I (Aslanoglou et al., 2006)

		Resolution				Linearity		
	fit	p_0	p_1 (GeV$^{1/2}$)	p_2 (GeV)	χ^2/ndf	a	b (GeV^{-1})	χ^2/ndf
Quartz Plate (S1, glass)								
Philips PMT	(1)	0.004 ± 0.002	0.36 ± 0.02		6.4/4	37. ± 12.	7.7 ± 0.2	4.2/4
	(2)	0.010 ± 0.004	0.38 ± 0.02	0.0 ± 0.4	7.4/3			
Adv. Photonix APD	(1)	0.017 ± 0.005	0.28 ± 0.04		2.5/3	32.5 ± 2.4	4.4 ± 0.1	2.2/3
	(2)	0.036 ± 0.006	0.24 ± 0.04	1.2 ± 0.2	6.2/2			
Quartz Fibres (S2, glass)								
Philips PMT	(1)	0.004 ± 0.003	0.45 ± 0.04		3.2/4	33.6 ± 9.7	4.6 ± 0.1	0.41/4
	(2)	0.013 ± 0.006	0.48 ± 0.02	0.0 ± 0.8	3.7/3			
Quartz Fibres (J2, glass)								
Adv. Photonix APD	(1)	-0.01 ± 0.01	1.16 ± 0.13		4.1/4	29.8 ± 3.3	1.4 ± 0.1	6.5/4
	(2)	0.04 ± 0.02	0.82 ± 0.22	4.5 ± 1.6	1.3/3			

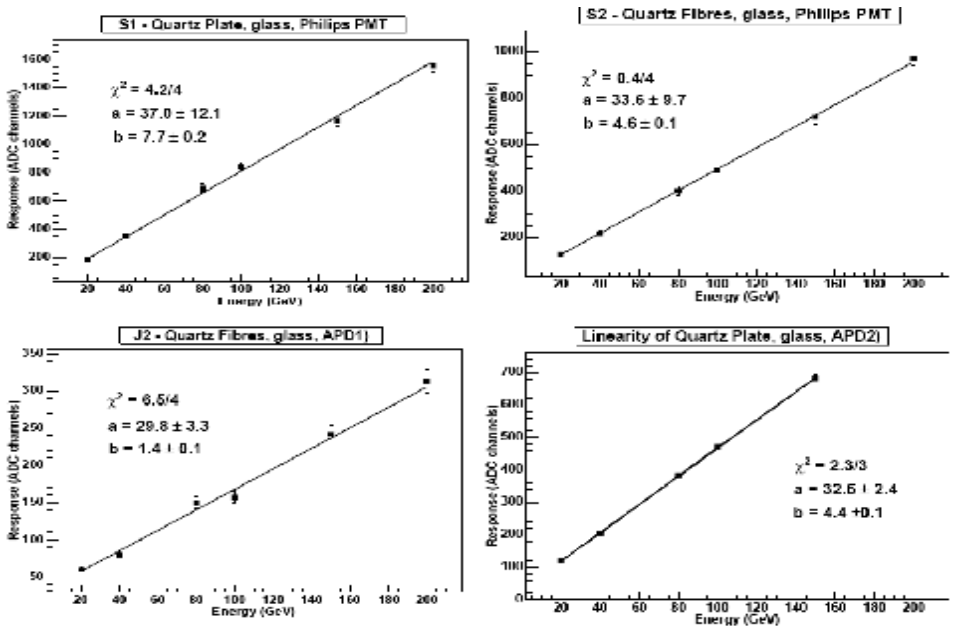


Figure 3.9. Energy linearity in different sectors: (a) S1 (Philips PMT), (b) S2 (Philips PMT), (c) J2(APD1), (d) S1 (APD2).

Relative energy resolution of the calorimeter was studied by plotting the normalized width of the Gaussian signal amplitudes (Figs. 3.5-3.8), σ/*E*, with respect to the incident beam electron energy, *E* (GeV) and the data points were fitted by two different functional forms:

$$\sigma/E = p_0 + p_1/\sqrt{E} \quad (3.2)$$

$$\sigma/E = p_0 \oplus p_1/\sqrt{E} \oplus p_2/E \quad (3.3)$$

the sign (⊕) indicates that the terms were added in quadrature. In expressions (3.2), (3.3) three parameters determine the energy resolution:

1. The constant parameter p_0, coming from the gain variation with changing voltage and temperature, limits the resolution at high energies.

2. The dominant stochastic parameter p_1, due to intrinsic shower photon statistics.

3. The noise p_2 parameter to contain the noise contribution from capacitance and dark current.

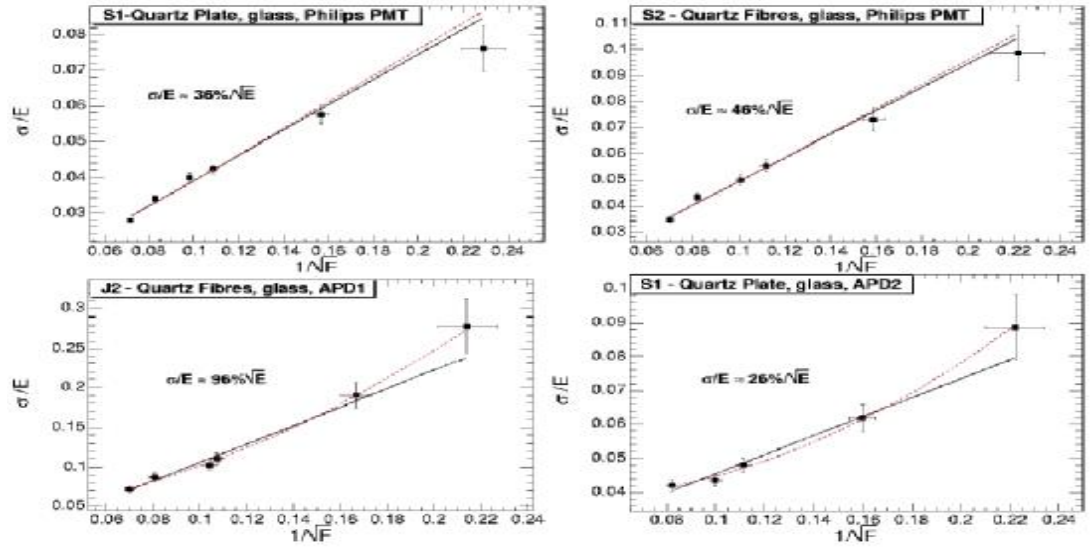


Figure 3.10. Energy resolution in sectors: (a) S1 (Philips PMT), (b) S2 (Philips PMT), (c) J2 (APD1), (d) S1 (APD2). Two fits are shown: eq. (3.2) (solid); eq. (3.3) (dashed), with E given in GeV.

Generally, both formulas satisfactorily fit the data (figure 3.10). The first constant term p_0 is close to 0 for all sectors. The average stochastic term p_1 was in the range ~26% – 96%. The p_2 term measured to be 1.25 GeV and 4.5 GeV for Advanced Photonix APD and Hamamatsu APD, respectively. The APDs were very sensitive to both voltage and temperature changes, but in this test there was no monitoring of their stability (Aslanoglou et al., 2006).

3.2. Prototype II and Beam Test 2004

The second performance study of the CASTOR calorimeter was with Prototype II. Beam tests were carried out with electrons, pions and muons in the H2 line at CERN/SPS in 2004. Prototype II was the first prototype to test the hadronic section of the calorimeter, it included both an electromagnetic (EM) and a hadronic (HAD) section, built in an octant geometry as in Figure 3.11. Its design was very close to the final design of the detector. Second prototype consisted of quartz plates, avalanche photodiodes (APDs) as well as photomultiplier tubes (PMTs), and air-core light guides with inner reflective foil (Dupont polyester film reflector coated with

AlO and reflection enhancing dielectric layer stack SiO2 +TiO2). The two types of PMTs used were Hamamatsu R7899 PMT, and radiation-hard PMT FEU-187 from RIE St. Petersburg, in with a cathode area of 2 cm^2. However the main difference from prototype I was a new semi-octant (φ=22.5) geometry of the readout unit in the EM section.

The EM and the HAD sections constituted one octant sector, both sections were constructed with successive layers of tungsten plates as absorber and fused silica quartz plates as active medium. The EM part was 14 cm long and divided into two semi-octant sectors, longitudinally segmented into 2 reading units, so that was 4 independent readout channels in total. HAD part was 40 cm long with the same octant geometry of prototype I. It was longitudinally segmented into 4 sections. The Cherenkov light produced by the passage of relativistic particles through the quartz plates was collected in reading units along the length of the calorimeter and focused by air-core light guides onto the photodetector (light-reading) devices, APDs or PMTs (Aslanoglou et al., 2007).

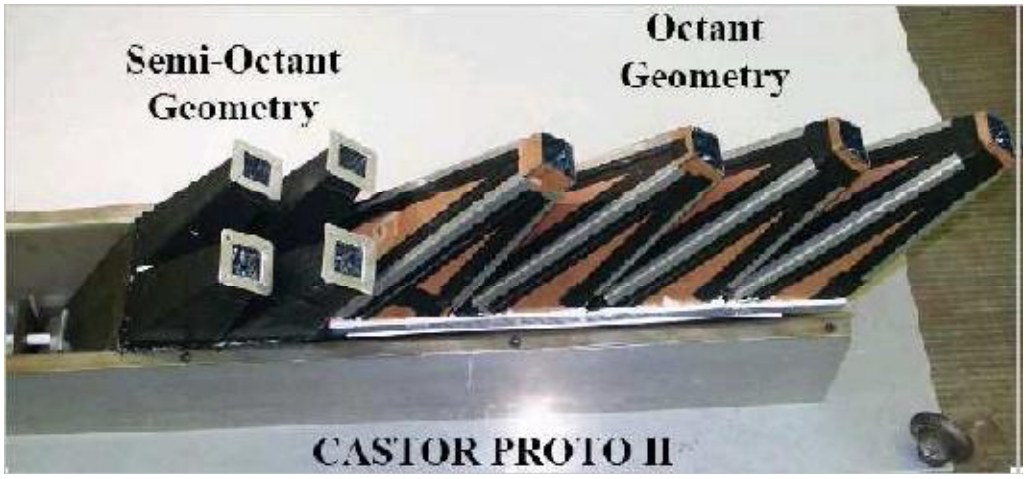


Figure 3.11. The CASTOR prototype II. Before assembling the light-reading devices. The semi-octant geometry of the EM section and the octant geometry of the HAD section (Aslanoglou et al., 2007).

The thickness of W-plates and Q-plates are respectively 3 mm and 1.5 mm for the electromagnetic section. However for the hadronic section, plates thicknesses

were different from the EM section, the W and Q-plates were 5 mm and 2 mm thick respectively. All the plates were inclined at 45° with respect to the direction of the impinging particles, in order to maximize the Cherenkov light output in the quartz. The perimeter sides of Q-plates were painted with white reflecting paint, except the top one. In the EM section, each Readout Unit (RU) consisted of 11 W/Q-plates layers corresponding to 13.4 X_0 (radiation length) or 0.536 λ_I (interaction length) depth. The total length of the EM section corresponded to 26.8 X_0 and 1.072 λ_I lengths. The readout units of the the hadronic section consisted of 10 W/Q-plates layers and were 0.796 λ_I depth, that was 3.186 λ_I in total. The whole prototype has 4.26 λ_I depth. For some runs with pions, an additional inactive absorber of 1.03_I was placed in front of the calorimeter, in order to make the EM section act as a hadronic one, increasing the total depth of the prototype to 5.3 λ_I (Aslanoglou et al., 2007).



Figure 3.12. View of the W/Q-plates of the EM and HAD sections (bottom pictures) and of the light guides (upper picture) in the semi-octant (octant) geometry of the EM (HAD) sections respectively of the CASTOR prototype-II (Aslanoglou et al., 2007).

3.2.1. Beam Test Results

Electron, hadron (π^-) and muon (μ^-) beams of several energies were used for the prototype II. The energy responses (linearity, resolution) of the electromagnetic and hadronic calorimeters were obtained with energy scans with: 20-200 GeV electrons, 20- 350 GeV pions, as well as 50, 150 GeV muons. The calorimeter prototype was placed on a platform movable with respect to the beam in both horizontal and vertical (x, y) directions. A telescope of finger scintillator detectors and wire chambers were installed upstream of the prototype, giving precise information on the position of each particle hitting the calorimeter

3.2.1.(1). Electron Beam

Electron beams with 20-200 GeV were used to test the energy linearity and resolution as well as the position resolution of the EM section.

3.2.1.(1).a. Energy Response

A typical spectrum measured with 100 GeV electrons incident on the EM section of the prototype, equipped with PMTs, is shown in figure 3.13. The electron beams also include muons that can be seen as minimum ionizing particle (MIPs) just above the pedestal. The energy response of the calorimeter was found to be Gaussian for all energies. Figure 3.14 shows the energy response for 20 and 200 GeV electron beams, obtained with 4 and 6 APDs respectively.

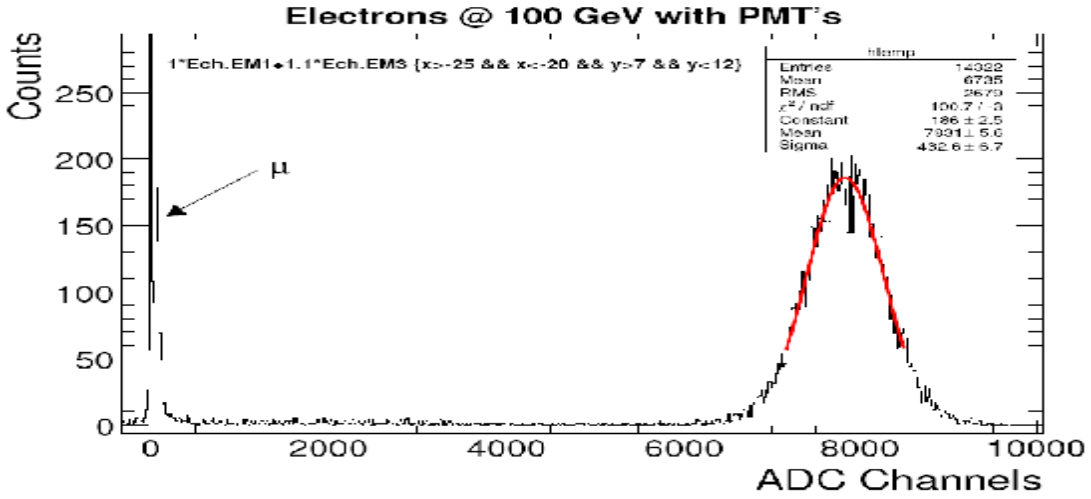


Figure 3.13. Energy response of the EM calorimeter equipped with PMTs to 100 GeV electrons. The muons signal can also be seen (Aslanoglou et al., 2007)

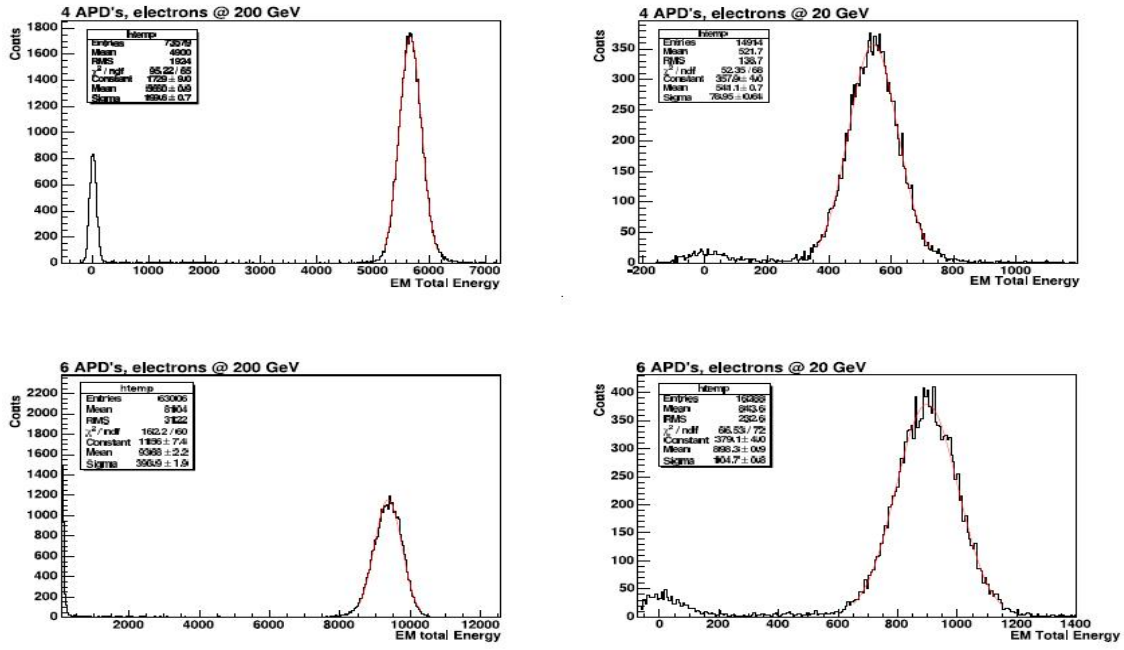


Figure 3.14. Electromagnetic spectra for different beam energies (200GeV and 20 GeV) for 4APD's and 6 APD's (Aslanoglou et al., 2007).

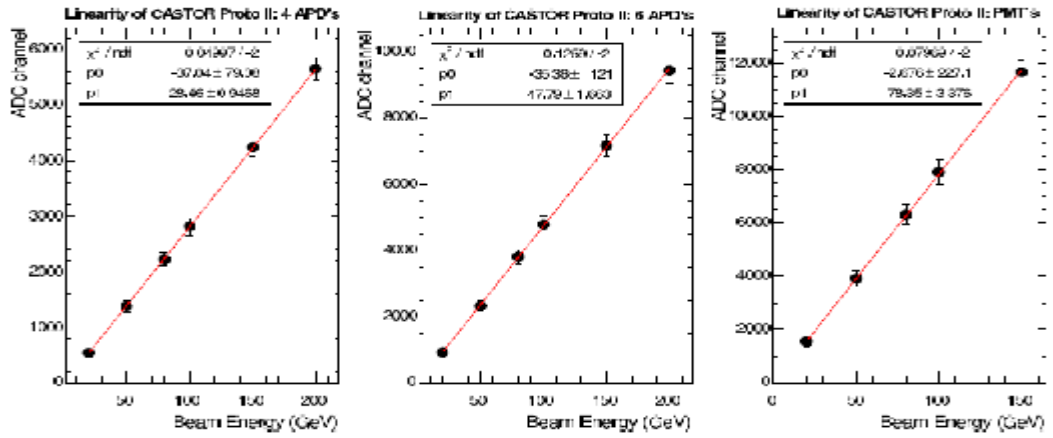


Figure 3.15. Energy response linearity (signal peak position versus beam energy) of the EM section, obtained with different light-reading devices: 4 APDs (left), 6 APDs (center), and PMTs (right) (Aslanoglou et al., 2007).

The response was found to be linear all the configurations, that was with PMTs or APDs. The constant term was found to be negligible while the signal amplitude was fitted by the formula (3.1)

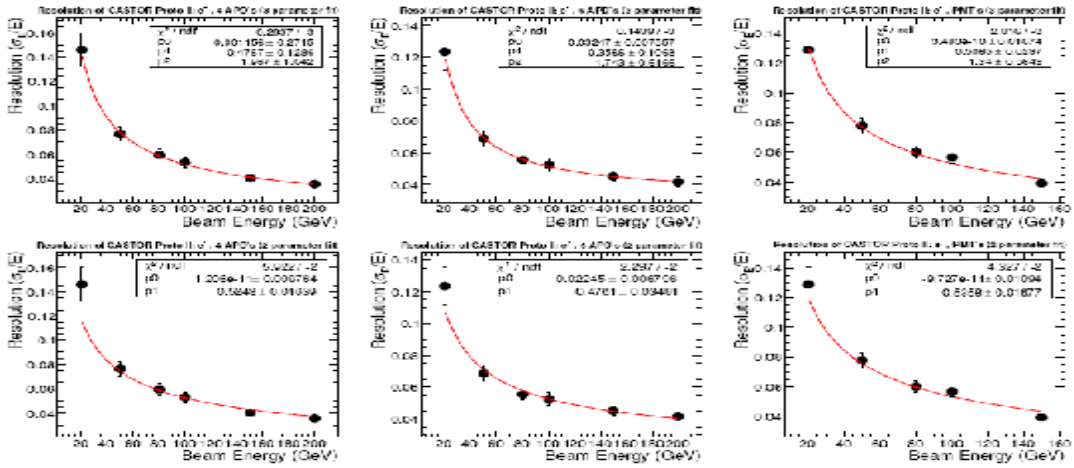


Figure 3.16. Energy resolution of the EM section, obtained with the three readout configurations considered: 4 APDs (left), 6 APDs (center), and PMTs (right): 3-parameters fit Eq. (3.3) (top); 2-parameters fit Eq. (3.2) (bottom) (Aslanoglou et al., 2007).

Figure 3.16 shows the results for all readout configurations considered. The stochastic term was measured in the range 36-51%, while the constant term was close to zero (Aslanoglou et al., 2007).

3.2.1.(2). Muon Beam

Muon energy spectra at 50 and 100 GeV were measured with the electromagnetic sector, using the PMT readout configuration. Figure 3.18 shows the muon peak measured for the 50 GeV beam well separated from the pedestal at zero counts. The line shape has been obtained with two different PMTs: Hamamatsu R7899 (fig. 3.17a), RIE FEU187 (fig. 3.17b). In figure (fig. 317c, the sum of both EM readout units is shown.

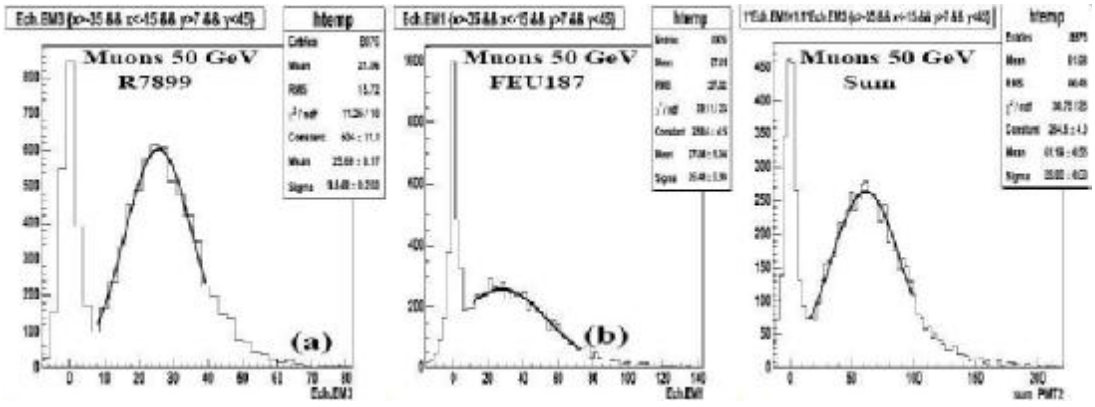


Figure 3.17. Energy spectra measured in the EM section of prototype II with a muon beam of 50 GeV energy and using two different PMTs: (a) Hamamatsu R7899, (b) RIE FEU187, and last one the sum of both (Aslanoglou et al., 2007).

Figure 3.17 shows that Hamamatsu R7899 PMT performs much better than the RIE FEU187 one, in identifying the muon signal above the pedestal. (Aslanoglou et al., 2007).

3.3. Prototype III and Beam Test 2007

Prototype III was tested in the H2 line at CERN Super Proton Synchrotron during two weeks in Aug-Sept 2007. The energy linearity, resolution and uniformity, as well as the spatial resolution were studied with electrons, pions and muons of various energies. The signal from muons, behaving as MIPs, was exploited for the inter-calibration of all the channels of the prototype. Other special studies included

runs with the beam hitting directly on the light-guides and PMTs and observing the readout response, as well as testing the light-output with an optimized Q–plate cut. The prototype was one full-length octant, including of the design EM and HAD sections, with a total of 28 readout-units (RUs) as shown in Figures 3.18 and 3.19, constructed with successive layers of tungsten (W) plates as absorber and silica quartz (Q) plates as active medium. The Cherenkov light, produced by the passage of relativistic particles through the quartz medium, is collected in sections of 5 W/Q layers along the length of the calorimeter and focused by air-core light guides onto the PMTs. The EM RUs 2 and 4 (left or Jura side) were equipped with RIE PMTs, whereas the rest of the RUs, and in particular all of the right or Saleve side, used Hamamatsu R5380O PMTs (Aslanoglou et al., 2008).

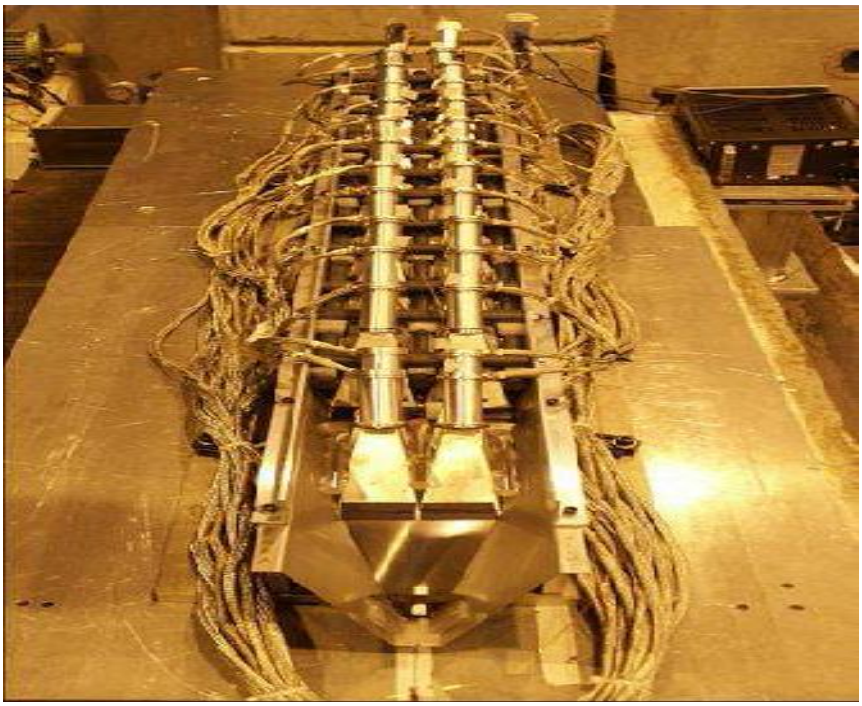


Figure 3.18. The fully instrumented CASTOR octant prototype III installed on top of the moving table at the CERN/SPS H2 line.

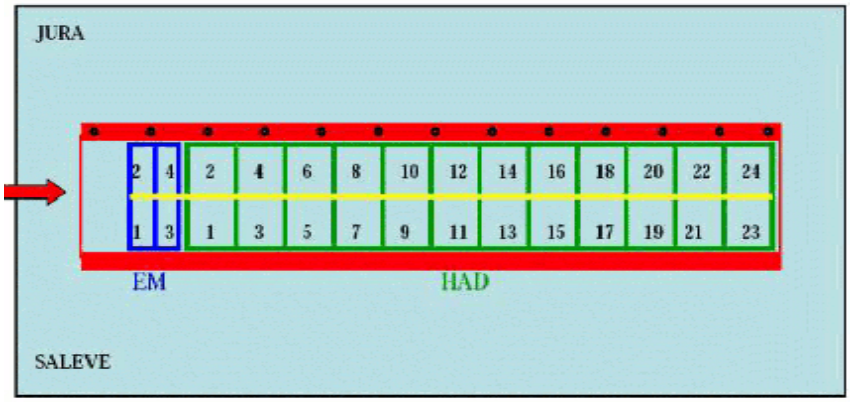


Figure 3.19. Schematic drawing of the beam-tests-2007 CASTOR prototype with the 28 readout units (RUs) indicated. The beam comes from the left impinging on the EM sections (Aslanoglou et al., 2008).

3.3.1. Muon Beam and Inter Calibrations of Channels

Muons of E = 50 GeV and E = 150 GeV were used for the intercalibration of the channels of the prototype III. Figures 3.20 and 3.21 show the muon peaks measured for the 150 GeV beam with the different PMTs. The muon signal was fitted by a Gaussian distribution. The signal was separated from the pedestal in the EM sections. After the replacement of the Q-plates in the first hadronic section of the Saleve side semi-octant that was equipped with the Hamamatsu PMT, the muon signal was also seen clearly in that channel. The good separation between the pedestal and the muon signal peak was exploited in order to intercalibrate the 28 channels of the calorimeter, by using the energy response per channel. Table 3.2 contains the derived intercalibration constants as obtained from the mean signal per channel and from a Gaussian+Landau fit of the muon signal peaks, also shown in Figure 3.22 (Aslanoglou et al., 2008).

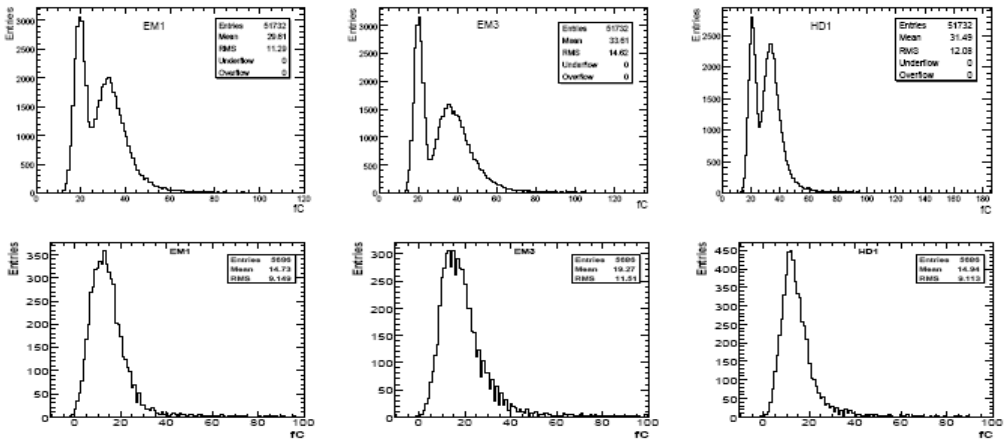


Figure 3.20. Energy spectra, before (top) and after (bottom) pedestal subtraction, measured in the two EM and first HAD sections of the prototype III with a muon beam of 150 GeV energy impinging on the Saleve semi-octant equipped with Hamamatsu PMTs (Aslanoglou et al., 2008).

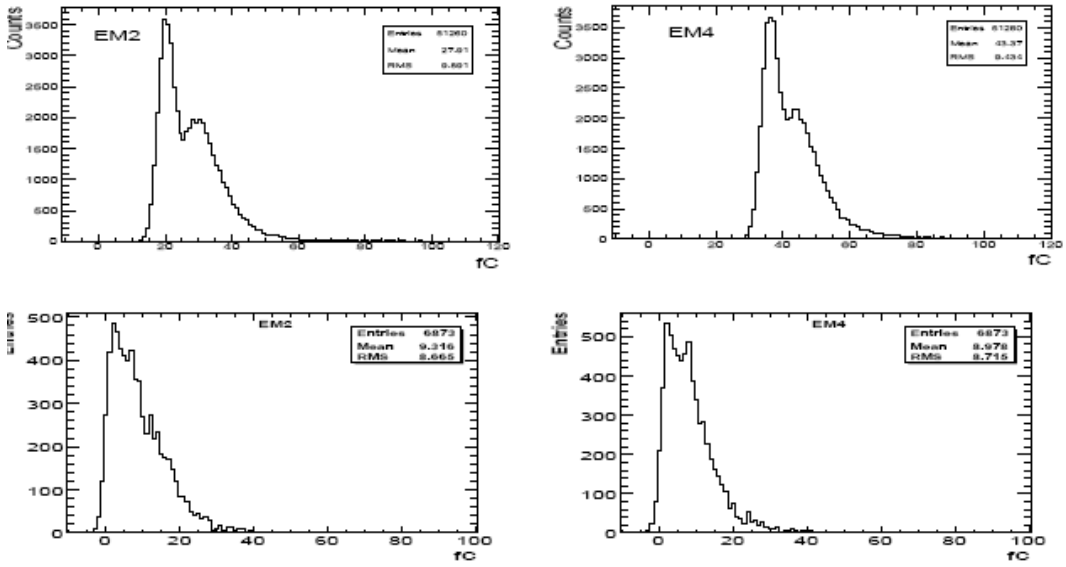


Figure 3.21. Energy spectra, before (top) and after (bottom) pedestal subtraction, measured in the EM section of the prototype III with a muon beam of 150 GeV energy impinging on the Jura semi-octant equipped with RIE FEU187 PMTs (Aslanoglou et al., 2008).

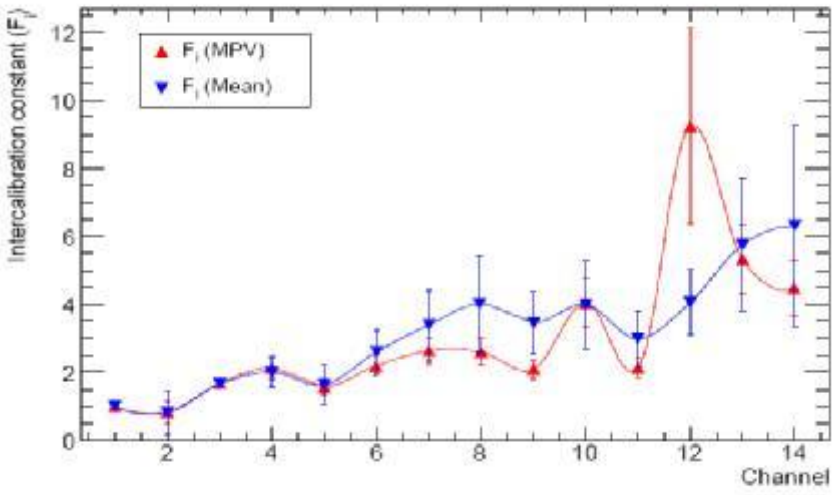


Figure 3.22. Intercalibration constants (F_i) of different channels in the Saleve side semi-octant, derived from the muon energy spectra (Aslanoglou et al., 2008).

Table 3.2. Inter-calibration constants for each channel, calculated using a run with a muon beam of 150 GeV (Aslanoglou et al., 2008).

Channel	F_i (MPV)	F_i $(Mean)$
EM1	1.0000 ± 0.0000	1.0000 ± 0.0000
EM3	0.8401 ± 0.0437 (stat)	0.8195 ± 0.0388 (stat) ± 0.0275 (syst)
HD1 (QP at 45^o)	2.5137 ± 0.3236 (stat)	2.4876 ± 0.5975 (stat) ± 0.2197 (syst)
HD1 (QP at 90^o)	1.6787 ± 0.0843 (stat)	1.6612 ± 0.1531 (stat) ± 0.0132 (syst)
HD3	2.3320 ± 0.3296 (stat)	2.0087 ± 0.400 (stat) ± 0.1862 (syst)
HD5	1.7247 ± 0.2188 (stat)	1.6339 ± 0.4033 (stat) ± 0.4093 (syst)
HD7	2.3881 ± 0.3108 (stat)	2.6066 ± 0.5417 (stat) ± 0.3011 (syst)
HD9	2.8879 ± 0.3649 (stat)	3.3910 ± 0.9397 (stat) ± 0.3564 (syst)
HD11	2.8547 ± 0.3797 (stat)	3.9939 ± 0.8160 (stat) ± 1.1854 (syst)
HD13	2.2996 ± 0.2950 (stat)	3.4543 ± 0.6627 (stat) ± 0.6220 (syst)
HD15	4.4350 ± 0.7447 (stat)	3.9887 ± 0.7839 (stat) ± 0.9968 (syst)
HD17	2.3320 ± 0.3007 (stat)	2.9906 ± 0.5818 (stat) ± 0.5614 (syst)
HD19	10.1370 ± 2.8787 (stat)	4.0573 ± 0.8707 (stat) ± 0.3940 (syst)
HD21	5.8437 ± 1.0153 (stat)	5.7573 ± 1.1246 (stat) ± 1.5886 (syst)
HD23	4.9180 ± 0.8443 (stat)	6.3119 ± 1.2647 (stat) ± 2.6950 (syst)

4. ANALYSIS AND RESULTS

4.1. Introduction

My analysis results of beam test 2008 of CASTOR Calorimeter Prototype IV are discussed in this part. Beam test data was taken in summer 2008 in the H2 line. The intercalibration constants for each channel (readout-units) were calculated by using two muon runs with E=300 GeV. Channels were not identical because of productivity and assembly, they have to be calibrated for a good analysis. So the intercalibration constants were calculated to eliminate the differences of calorimeter's response.

4.2. The H2 Beam Line

Muon, electron or hadron beams of energies between 10 GeV and 350 GeV, as well as 400 GeV protons are provided as secondary particle beams. The beam test of prototype IV was performed on H2 beam line. It was fixed on platform movable in both horizontal and vertical (x, y) directions. A schematic description of the H2 beam line of the Super Proton Synchrotron SPS at CERN is shown in figure 4.1.

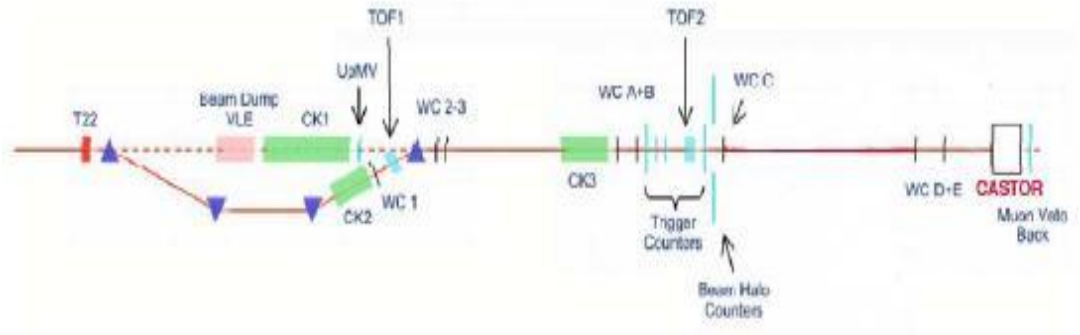


Figure 4.1 Schematic figure of the H2 beam line of the SPS at CERN (Aslanoglou et al., 2008).

A production target (T2) is placed 590 m far from the prototype to produce different particles such as muons, electrons and pions with momentum range between 10 Gev/c and 350 Gev/c. Target T22 was located 97 m upstream of the prototype in order to produce very low energy (VLE) particles with momentum range between 1 and 9 GeV/c. There were eight wire chambers in the beam line but only WC-A, WC-B, WC-C, WC-D, WC-E were used for CASTOR calorimeter (figure 4.2). Wire chambers, giving information on the position of each particle hitting the calorimeter, were placed upstream of the prototype. The spatial resolution is about 350 μm in both *x* and *y* coordinates.

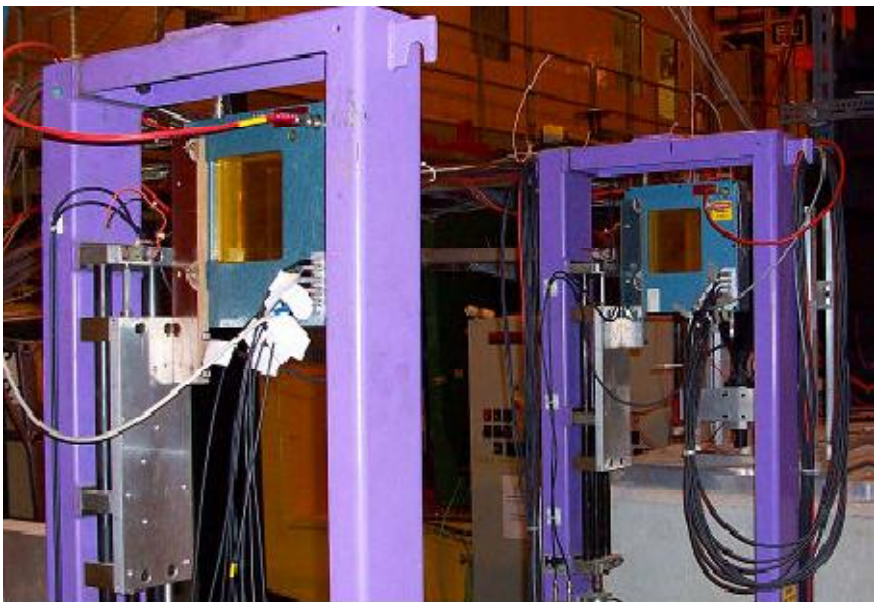


Figure 4.2. WC-C and WC-D (Tali, 2009).

Three Muon Veto counters were used; Muon Veto Front (MVF), Muon Veto Back (MVB), and Muon Veto Wall (MVW) couters. The MVF and MVB were scintillation counters. They were placed well behind the calorimeters. Also, MVB was located behind the calorimeter and was used to tag muons (figure 4.3).

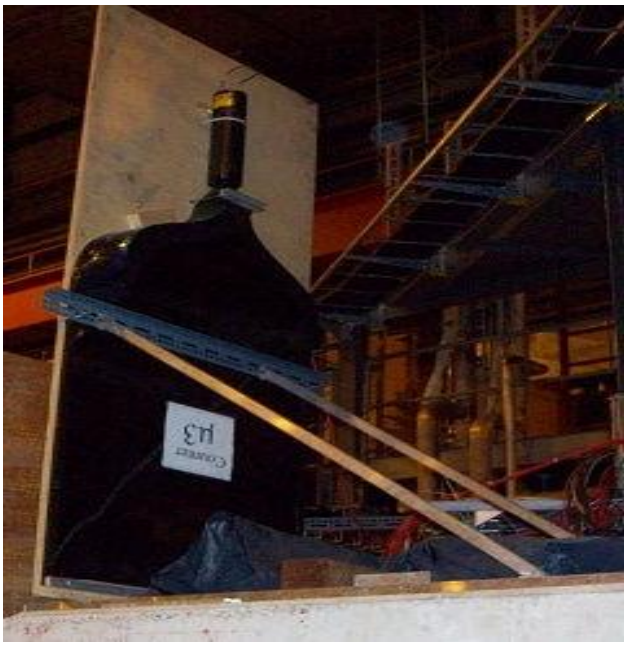


Figure 4.3. A view of MVB (Tali, 2009).

Four scintillation counters (S1 through S4) were used for triggering. The beam trigger typically consisted of the S1, S2, S3 and S4 which defined a 4x4 cm^2 area on the front face of the calorimeter. S3 had a problem. Because the S4 counter gave a clean pulse height distribution of single and multiple particles in the beam, S4 was used to eliminate multi-particle events off-line. Figure 4.4 shows S1,S2, and S4.



Figure 4.4 A view of sicintilation counters S1, S2 and S4 (Tali,2009).

There were two Cherenkov counters (CK2 and CK3) in the very low energy mode and in the high energy mode in order to identify particles. Also, there were two time of flight counters (TOF1 and TOF2) which are able to separate lighter and heavier fundamental particles.

4.3 Beam Test 2008 of Prototype IV

Prototype IV was constructed and tested in summer 2008 in the H2 line at CERN/SPS. Channel intercalibration, gain variation and pedestals of the channels were studied with muon beams. Resolution, uniformity, energy linearity and the surface scan were analyzed by using the electron, pion and muon beams at various energies.

The prototype IV was a full-length octant that had 28 Readout-Units RUs). These channels consisted of electromagnetic (EM) and hadronic (HAD) sections. As seen in figure 3.18, tungsten (W) plates and quartz (Q) plates were placed in one octant of Castor prototype-IV. The Cherenkov light, produced by the passage of relativistic particles via the quartz medium, is collected in sections of 5 W/Q layers along the length of the calorimeter and focused by air-core light guides onto the PMTs. Also a schematic drawing of the beam test with 28 RUs indicated are shown in Figure 3.19. Details of the prototype-IV were given in the second chapter.

4.3.1. Muon Beam and Intercalibration

Muon energy spectra between 50 GeVand 350 GeV were measured in the EM and HAD sections. In this analysis, muon beams were used since muons move along detector without losing all of their energies. Two muon runs were selected within other runs for this analysis. These runs had the most events (50k) and hit to the center of semi-octant of calorimeter (one of runs hit Salve sector, another one hit Jura Sector). Table 4.1 shows properties of the muon runs which were used to calculate the intercalibration constans.

Table 4.1. Properties of muon runs

Run number	**Energy** (GeV)	**Events**	**X position** (mm)	**Y Position** (mm)	**Beam Sector**
48849	300	50k	-20	0	Saleve
48835	300	50k	-50	1	Jura

It is important to know the behaviour of beam and Scintillation counter let us know whether there is a real beam or not. When there is a real beam, the data from scintillation counter will be used as a trigger. Also, they were used to select the single hits and eliminate multi-particle events off-line. A gauss fit was applied over the first peak within 3 sigma to select events which had a single hit. So events around these values were kept events that have multiple hits were rejected. S1,S2 and S4 signals are shown in figures 4.5 and 4.6 for two runs (48849 and 48835) respectively.

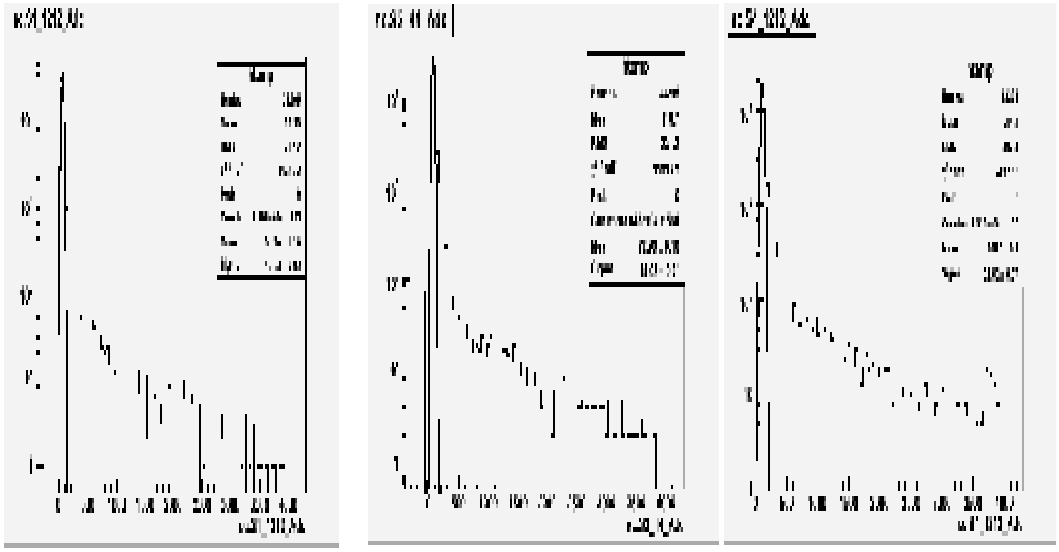


Figure 4.5 ADC distribution of scintilation counters S1 & S2 & S4, first peak was fitted by a Gaussian for #48849.

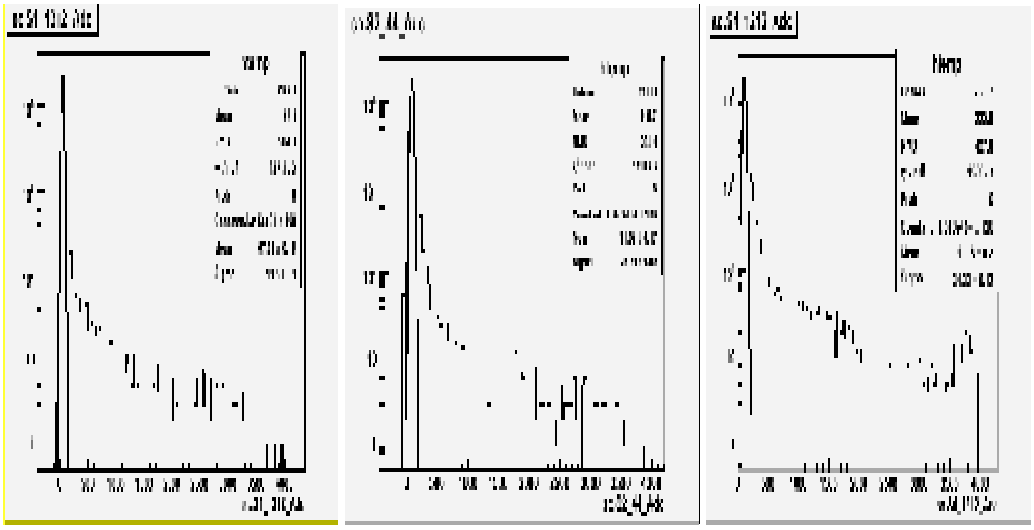


Figure 4.6. ADC distribution of scintilation counters S1 & S2 & S4, first peak was fitted by a Gaussian to select single hit for #48835.

Another important thing was to know the beam position. WC information gave us the beam position. We had to choose one WC worked well. As shown in figures 4.7 and 4.8, WC-A was not working, and WC-B, WC-C and WC-D were not good because there are more missing events on them. The distribution of the particles

in the WC-E was the best, moreover it is the closest to prototype. So WC-E was chose to use in this analysis. Figures 4.7 and 4.8 show WC information for runs 48849 and 48835 respectively.

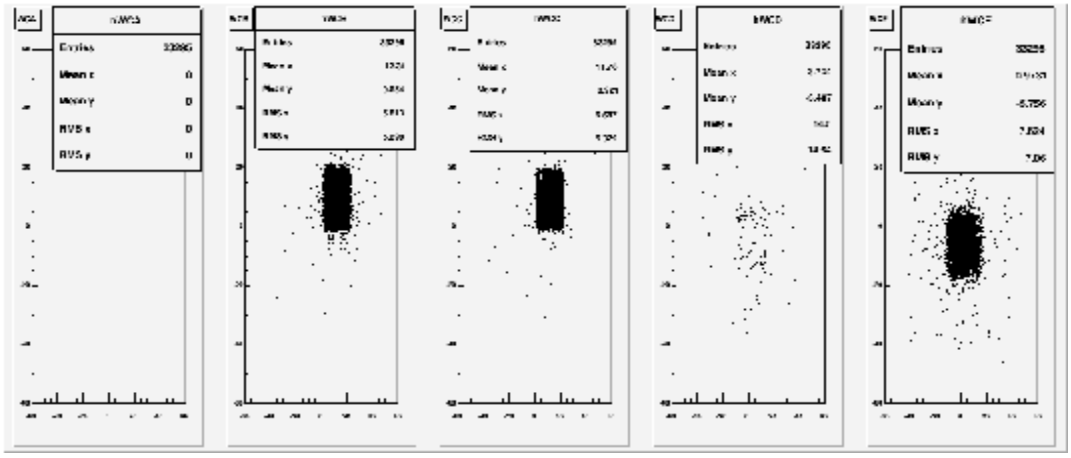


Figure 4.7. WC information for run # 48849 (Saleve sector).

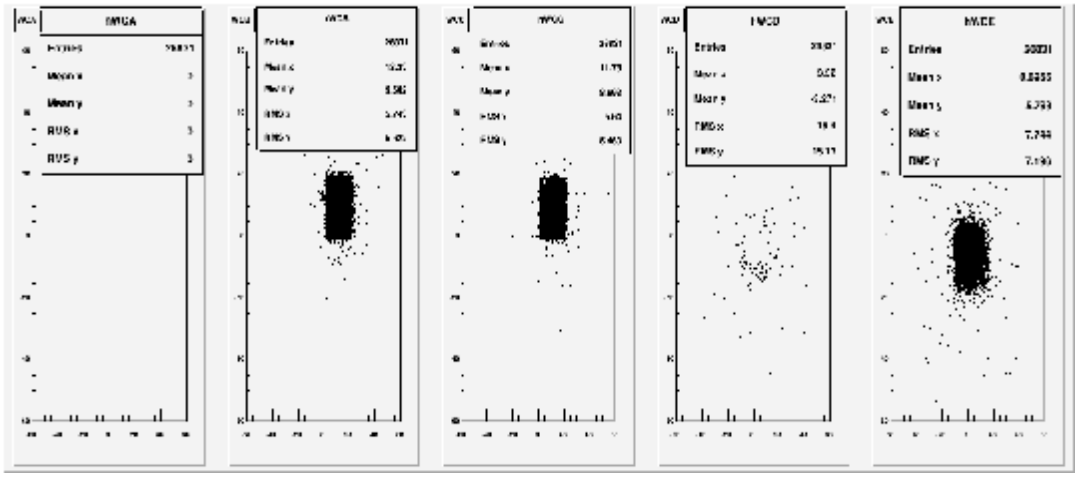


Figure 4.8. WC information for run # 48835 (Jura sector)

To identify muons, scintillation information and Muon Veto Back (MVB) counter were used. MVB information with the pedestal trigger had been used to determine the muon peak, this information was used in the beam trigger to define

muons. Figures 4.9 (for run #48849) and 4.10 (for run#48835) show the MVB pedestal signals.

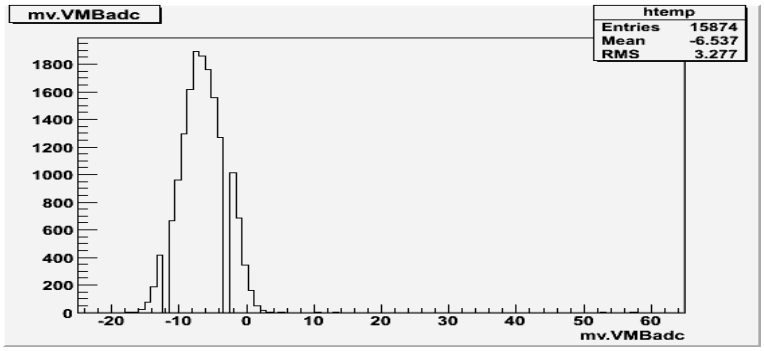


Figure 4.9. ADC distribution of the MVB signals with pedestal trigger for run #48849).

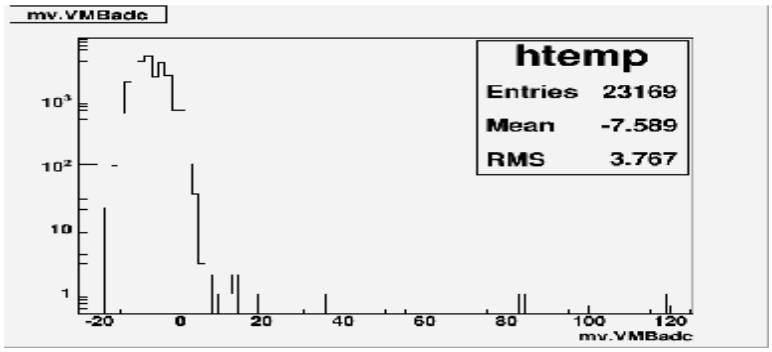


Figure 4.10. ADC distribution of the MVB signals with pedestal trigger for run #48835).

The muon, pion or electron beams include some other particles and beams need to be cleaned of them. The beams are not exactly clean. So some standard cuts were applied in this analysis to reject the unwanted particles (electrons, pions).

The cuts were applied for runs (48849 and 48835):

Radius cut: A 5 mm radius cut was applied around the beam center. Also for this cut, WC-E information was used. Figures 4.11 (for run #48849) and 4.12 (for run #48835) show beam profiles. The left plots have not any cuts and the right one has the radius cut with WC-E info.

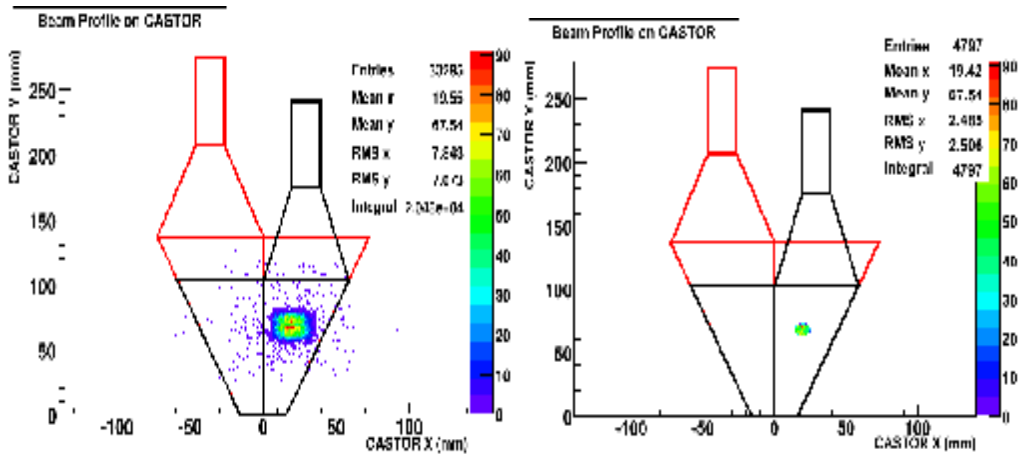


Figure 4.11. For run #48849, beam profile onto the front face of the semi-octant calorimeter (Saleve sector) using the hits distribution from the WC-E, the left plot has not radius cut and the right one has 5 mm radius cut.

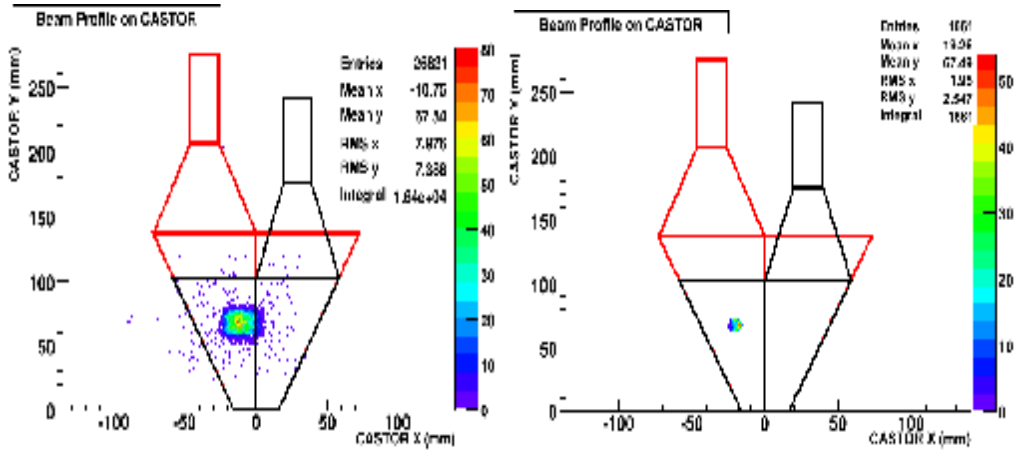


Figure 4.12. For run #48835, beam profile onto the front face of the semi-octant calorimeter (Jura sector) using the hits distribution from the WC-E, the left plot has not radius cut and the right one has 5 mm radius cut.

Muon Veto cut: Muon Veto cut was applied to select muons and reject other particles. MVB information (mean+3sigma) with pedestal trigger was used in the beam trigger to select muons.

Single hit cut: Single hit cut was applied by using WC-E and scintillation counter information.

Muon Energy distributions at 300 GeV were measured in each EM and HAD sections. After applying these cuts, exactly clean muon peaks were obtained for each RUs of the prototype. The muon peaks were fitted to a Gaussian+Landau (Langaus) distribution as seen below. The muon signal was also seen clearly in those channels. The good pedestal separation allowed us to use the fitted muon signal for intercalibration of all channels of the Prototype IV. Energy distributions in ADC counts of some channels (two EM and first two HAD channels) are shown below in figures 4.13,4.14, 4.15 and 4.16.

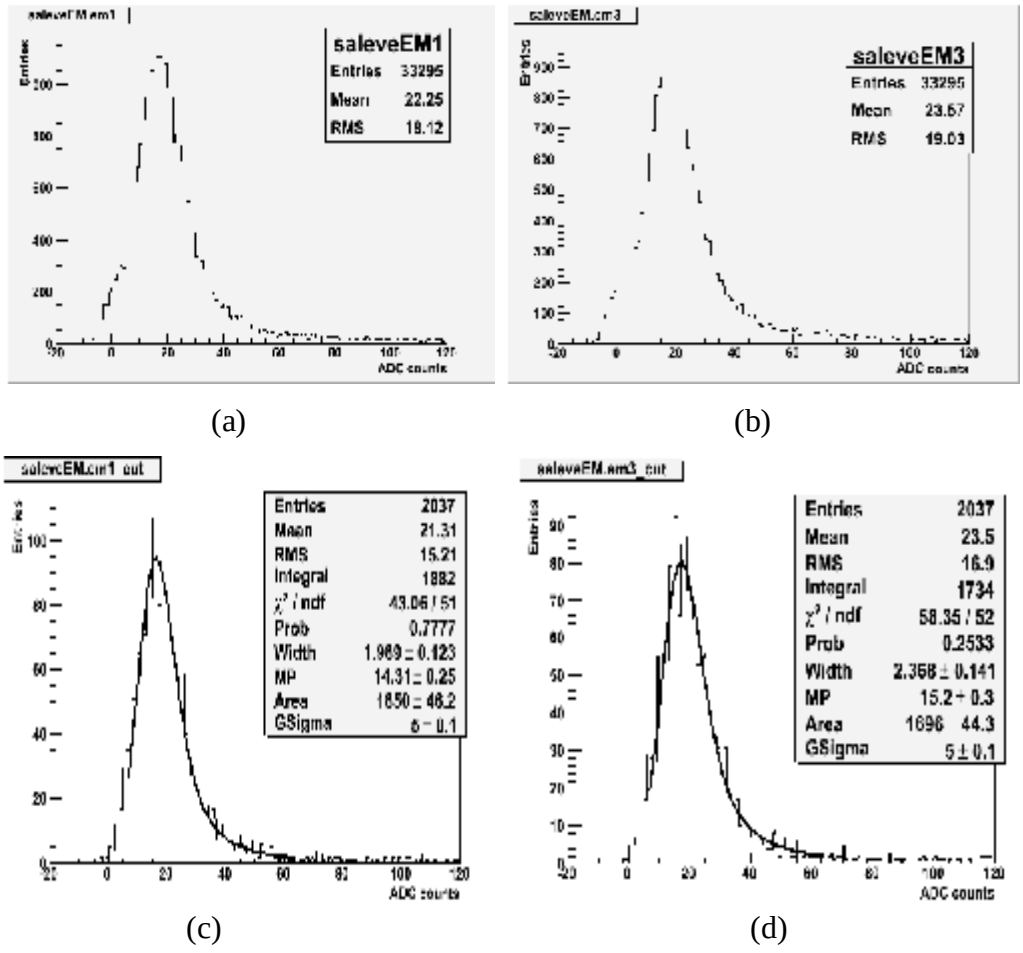
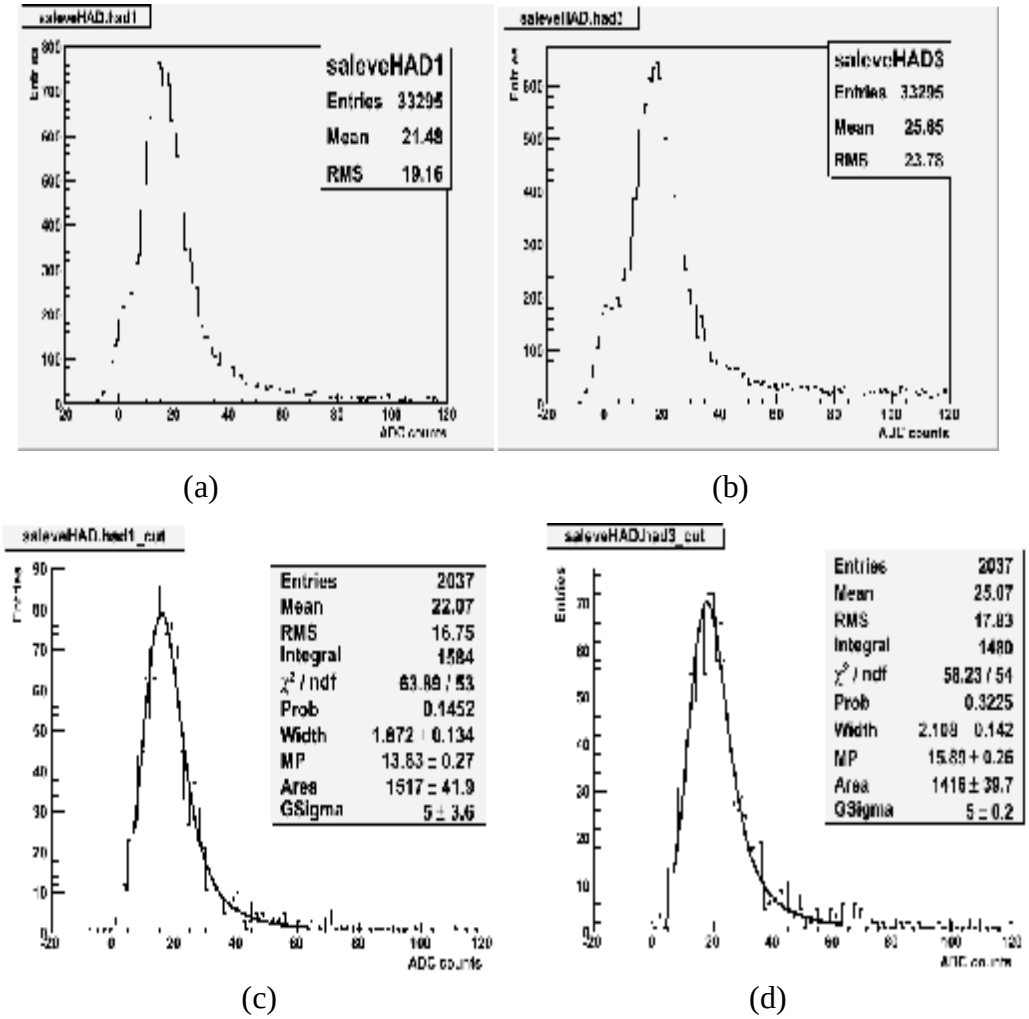


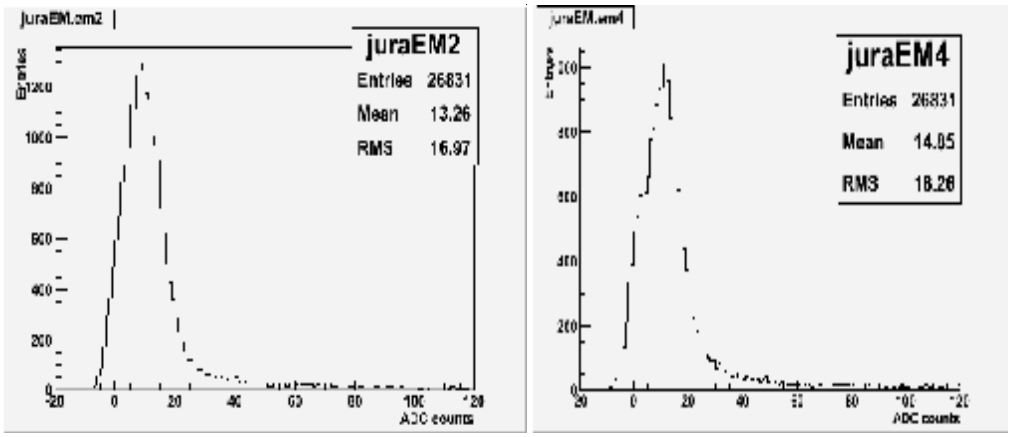
Figure 4.13. Energy distribution, before cuts (a, b) and after cuts (c,d), measured in the two EM channels of prototype IV with a muon beam hitting on the semi-octant (Saleve sector) for run #48849.



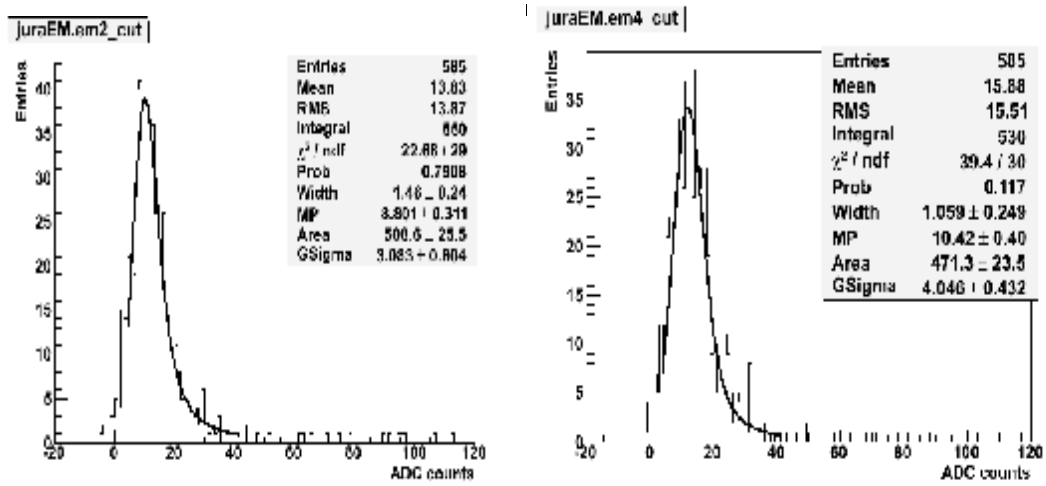
(a) (b)

(c) (d)

Figure 4.14. Energy spectra, before cuts (a, b) and after cuts (c, d) , measured in the first two HAD channels of prototype IV with a muon beam hitting on the Saleve side semi-octant for run #48849.



(a) (b)



(a) (d)

Figure 4.15. Energy distribution, before cuts (a ,b) and after cuts (c, d) , measured in the two EM channels of prototype IV with a muon beam hitting on the Jura Side side semi-octant for run #48835.

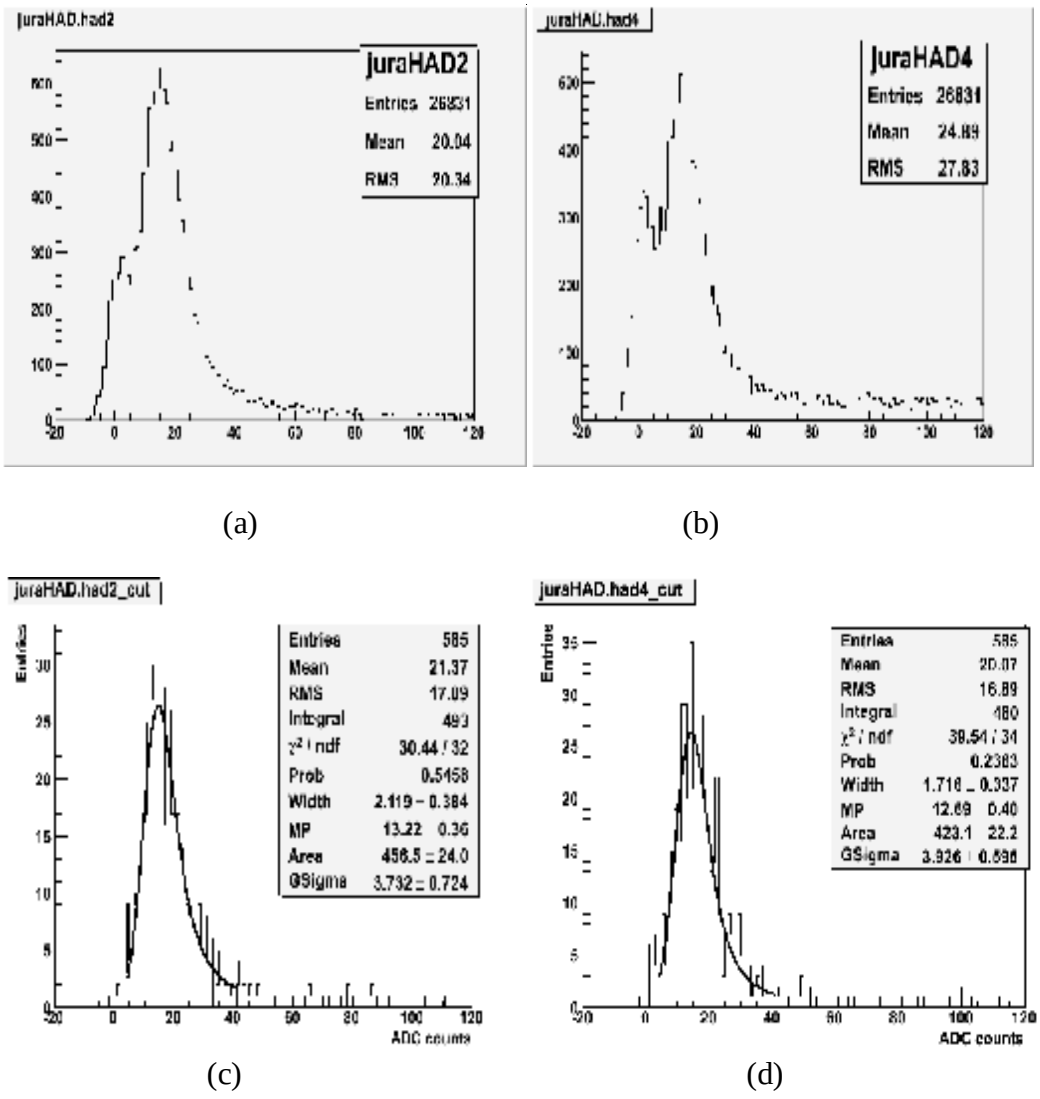


Figure 4.16. Energy distribution, before cuts (a, b) and after cuts(c, d), measured in the first two HAD channels of prototype IV with a muon beam hitting on the Jura side semi-octant for run #48835.

.

The channel response to muons was used to calculate the intercalibration constants, from the following formula:

$$F_i = E_1/E_i \times C_{\text{absorber}} \times C_{\text{QP cut}} \quad (4.1)$$

where E_1 is the response (the mean value of the energy distributions in ADC counts) of first EM channel in the sector used (Saleve or Jura), E_i is the response of the calorimeter in ADC counts for channel i, C_{absorber} could have different values 1 or 2 for EM and HAD channels because of the differences of Q and W Plates of thickness as given equation (4.2).

$$C_{absorber} = \begin{cases} 1, \text{for EM} \\ 2, \text{for HAD} \end{cases} \quad (4.2)$$

and

$$C_{QPcut} = \begin{cases} 1, & \text{for channels with Q} - \text{Plates cut at } 90^{\text{O}} \\ \dfrac{G(\pi)}{G(\mu)}, & \text{for channels with Q} - \text{plates cut at } 45^{\text{O}} \end{cases} \quad (4.3)$$

where G(p), $G(\mu)$ is the light gain for the transition after the change of the Q-plates for pions and muons respectively. C_{QPcut} has two different values according to the plate cuts at different angles as shown in equation (4.3). Because of the plates cut at 90^{o} in Prototype IV, $C_{\text{QPcut}}=1$ is used in equation (4.1)

The calculated intercalibration constants for each channel are in the table 4.2 and shown in figure 4.17 for Saleve side. Table 4.3 and figure 4.18 are for Jura side.

Table 4.2. Intercalibration constants for each channel, calculated using a run with a muon beam of 300 GeV and equation 4.1 F_i (MPV) corresponds to a Gaussian+Landau fit of the spectra for Saleve side

Channels (RUs)	F_i
EM1	1
EM3	0,9527
HAD1	2,0694
HAD3	1,8011
HAD5	1,9272
HAD7	2,3174
HAD9	1,5742
HAD11	1,8206
HAD13	2,3712
HAD15	2,2750
HAD17	2,0487
HAD19	2,2732
HAD21	1,4506
HAD23	3,5681

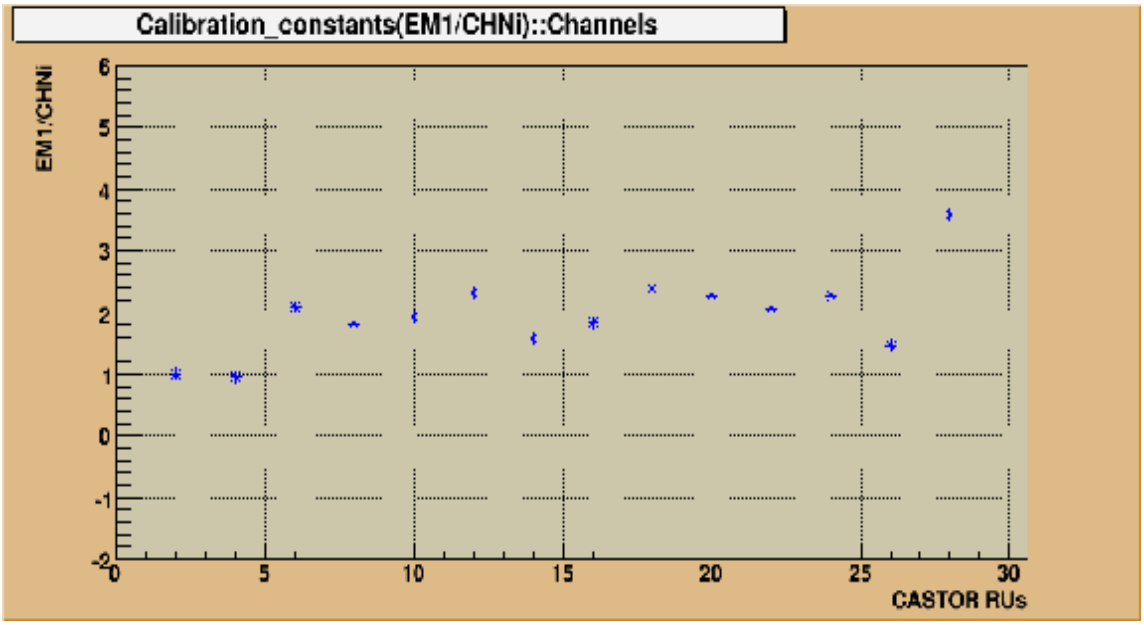


Figure 4.17. Intercalibration constants (F_i) of different channels in the Saleve side semi-octant, derived from the muon energy spectra.

For Jura sector, calibration constants were calculated for 12 channels because the last two HAD channels (HAD 22 and HAD 24) were not working.

Table 4.3. Intercalibration constants for each channel, calculated using a run with a muon beam of 300 GeV and equation 4.1 F_i corresponds to a Gaussian+Landau fit of the spectra for Jura side

channel	F_i
EM2	1,6260
EM4	1,3733
HAD2	2,1649
HAD4	2,2553
HAD6	2,4822
HAD8	1,7537
HAD10	3,4716
HAD12	4,1376
HAD14	3,4284
HAD16	2,7519
HAD18	4,0851
HAD20	4,5085

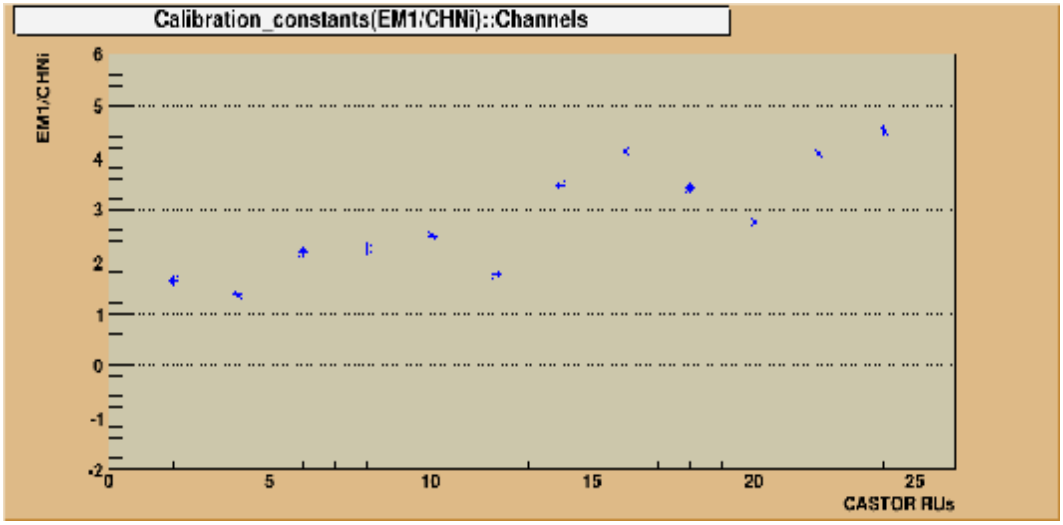


Figure 4.18. Intercalibration constants (F_i) of different channels in the Jura side semi-octant, derived from the muon energy spectra

5. CONCLUSION

The data were taken during the test beam 2008 in the H2 CERN/SPS beam line and the performance studies of the CASTOR calorimeter Prototype IV were carried out with this data. The ROOT and CMSSW software were used while performing the analysis. This thesis especially focuses on each channel of Prototype-IV. The intercalibration constants were calculated in order to eliminate the differences of calorimeter's response coming from the production and assembly of each channel.

Some cuts were applied for better results in this analysis, using the ADC information of the downstream wire chambers, as well as cuts were applied to both EM and HAD channels of the prototype-IV that made possible the study of muon beams by eliminating electrons, pions and pedestal which contaminate in the beam. After the cuts on the beam profile, the muon peaks were observed to be well fitted by Gaussian+Landau distributions. The muon peaks were clearly separated from the pedestal with the MVB cut. Some plots, with applied cuts are seen in figures from 4.13 (c, d) to 4.16 (c, d).

It is seen in figure 4.17 that the prototype IV exhibits better linearity on Saleve sector (for run # 48849) than Jura sector for (run # 48835). The measured intercalibration constants for every channel are in table 4.2 and seen in figure 4.17 for Saleve sector. Using the intercalibration constants on Saleve sector gave more consistent results.

Due to the different characteristics of the final prototype IV, with respect to the previous prototypes tested in previous beam tests, direct matching can not be easily made between the various studies because of the fact that every prototype has been tested for different aims. The measures of the tungsten and quartz plates were not the same therefore the act of the prototype IV can not be compared in definite values, as well as the geometry of the light-guides, but we can say that each constituent of prototype IV was working well and the calorimeter prototype IV settled the final design for the CASTOR calorimeter.

REFERENCES

AKGUN, U., 2003. CMS HF Calorimeter PMTs and Ξ^{+}_{c} Lifetime Measurement. University of Iowa, USA (PH.D,Thesis)

ASLANOGLOU et al., 2006, First performance studies of a prototype for the CASTOR forward calorimeter at the CMS experiment, CMS-NOTE 2006-142.

ASLONLOGLOU et al., 2007, Performance Studies of Prototype II for the CASTOR forward Calorimeter at the CMS Experiment, arXiv:0706.2641v2 [physics.ins-det].

ASLANOGLOU et al., 2008, Performance studies of the final prototype for the CASTOR forward calorimeter at the CMS experiment CMS NOTE 2008/- (in preparation)

CASTOR Engineering Design Report (EDR), 2007, CERN

CMS Physics Technical Design Report, 2007, Vol II, CERN

GLADYSZ-DZIADUS, E., 2006. CASTOR: Centauro And Strange Object Research Exotic Aspects of Forward Physics, Acta Physica Polonica B.

GUMUS K.Z., 2008, Search for New Physics in the Compact Muon Solenoid(CMS) Experiment and the Response of the CMS Calorimeters to Particles and Jets. Texas Tech University. PH.D Thesis.

MOORTGAT, F., 2004. Discovery Potential of MSSM Higgs Bosons Using Supersymetric Decay Modes with the CMS Dedector. Universiteit Antwerpen, Wetenchappen. PH.D. Thesis.

NORBECK, E. et al., 2006. Physics at Very Small Angles with CASTOR at CMS. 22nd Winter Workshop on Nuclear Dynamics.

PANAGIOTOU, A.D., 2008. CASTOR a novel calorimeter at very forward CMS Enhancing forward Physics. ICPP_CMS-CASTOR Status_281008.

TALİ, B.,2009. Test Results of the Hamamtsu R7378a Phototubes, Analysis of the Test Beam 08 and Preliminary After-Installation Data of the CMS-CASTOR Calorimeter. University of Çukuova. PH.D. Thesis.

www.en.wikipedia.org/wiki/Particle_physics

www.infao5501.ag5.mpi-sb.mpg.de:8080/topx/archive?link=Wikipedia-Lip6-2/23259.xml&style

www.particleadventure.org/electroweak.html

www.www.particlephysics.ac.uk/explore/atoms-and-particles.html

www.en.wikipedia.org/wiki/CERN

www.public.web.cern.ch/public/en/LHC/LHC-en.html

www.public.web.cern.ch/public/en/LHC/LHCb-en.html

www.public.web.cern.ch/press/PressReleases/Releases2008/PR14.08E.html

www.press.web.cern.ch/press/PressReleases/Releases2008/PR08.08E.html

www.cms.web.cern.ch/cms/index.html

www.public.web.cern.ch/public/en/LHC/ATLAS-en.html

www.public.web.cern.ch/public/en/LHC/LHCb-en.html

CURRICULUM VITAE

I was born in Ceyhan in 1981. I graduated from primary, secondary and high school in Ceyhan. I enrolled to the Physics Department in Çukurova University and I graduated in 2004. After my bachelor degree, I continue to study for my Master in High Energy Physics, at Institute of Natural and Applied Sciences in Çukurova University.